# DEVELOPMENT OF SOLID ELECTROLYTE MATERIAL BASED ON ZIRCONIA – BISMUTH OXIDE

*Thesis submitted in partial fulfilment of the requirement for*

*The award of the degree of*

**Master of Technology (M. Tech)**

In

**MATERIALS AND METALLURGICAL ENGINEERING**


Submitted by

**PARAMJYOT KUMAR JHA**

**Roll No. : 600802013**

Under the guidance of

**Dr. O.P PANDEY**

Head of the Department

School of Physics & Materials Science



School of Physics & Materials Science

Thapar University, Patiala


**July 2010**

*Dedicated To My Loving*

*And Caring Guide*

## CERTIFICATE

This is to certify that this thesis entitled **"DEVELOPMENT OF SOLID ELECTROLYTE MATERIAL BASED ON ZIRCONIA - BISMUTH OXIDE"** submitted for partial fulfilment of the degree of master of technology in the subject of material science and metallurgy of the Thapar University, Patiala, is a bonafide research work carried out by Mr. **Paramjyot Kumar Jha** under our supervision and that no part of this thesis has been submitted for any other degree.


**(Dr. O. P. Pandey)**
Professor and Head, SPMS
Thapar Institute of Engg. & Technology,
Patiala, Punjab (147004)

**(Dr. R.K Sharma)**
Dean, Academic Affairs
Thapar Institute of Engg. & Technology,
Patiala, Punjab (147004)

# ACKNOWLEDGEMENT

I express my deep gratitude and respects to my guide and mentor **Dr. O.P. Pandey, Professor and Head, School of Physics and Materials Science** for his keen interest and valuable guidance, strong motivation and constant encouragement during the course of the work. I thank him from the depths of my heart for introducing me to the area of solid oxide fuel cells. I thank him for his great patience, constructive criticism and myriad useful suggestions apart from in valuable guidance to me. My first and foremost offering of thanks goes to the architect who shaped my dreams into reality.

My greatest thanks to **Dr. Kulvir Singh, Associate Professor and PG Incharge, School of Physics and Materials Science** for his encouragement and execution of thesis work. Their meticulous attention towards my proceedings, their devoted time and their ideas has enabled me to make the project a success. Their faith in me has always made me more confident. Their blessing always made me optimistic. It had been my privilege to work under their guidance.

My special thanks to **Miss. Jasmeet Kaur Gill (Research Scholar)** for her guidance in whole project work. She helped me in all stages during the course of my work. Without whom this project work cannot be completed.

My greatest thanks **Mr. Akshay Kumar (Research Scholar)** for his assistance and partnership were of great pleasure. His comments and views were very insightful and helpful.

I would also like to thanks **Dr. K.K. Raina, Professor and Deputy Director, School Of Physics and Materials Science** for his guidance and encouragement of thesis work. I am also thankful to **Dr. D.P. Singh, Dr. Puneet Sharma,** and all the faculty members of

School of Physics and Materials Science for their constructive suggestions at different stages of this work. I really very thankful from my heart to all **(Research Scholars) Mr. Vishal Kumar, Mr. Ravi shukla, Mr. Kapil Sood, Mr. Ranvir Singh, Ms. Kamalpreet Kaur, Mrs. Bhupinder Kaur, Mrs. Gurbinder Kaur,** and all other **Phd. Scholars** for his assistance, suggestions and partnership were of great pleasure. There comments and views were very insightful and helpful.

My sincere thanks to Lab supdt. (SPMS), **Mr. Purshottam** for his help to carry out X-Ray diffraction and SEM studies.

I would also like to thank **Mr. Jant Singh** for providing all kind of assistance in PG Lab for creating a healthy research environment.

I would like to convey my sincere gratitude to my friends and colleagues **Ram Kishor, Gaurav Singla, Rajni Sharma, Sumit Bharadawaj, Rashmi Mittal, Poonam Sharma, Ritesh kumar, Poonam Benjwal, Alok Mishra,** for their support, co-operation and their timely help and valuable discussions.

I owe my sincere thanks to all the staff members of School of Physics and Materials Science for their support and encouragement. The meaning of my life and work is incomplete without paying regards to my respected parents whose blessings and continuous encouragement have shown me the path to achieve my goals. And above all, I pay my regards to the **Almighty** for his love and blessings.

Paramjyot kumar Jha.

Paramjyot kumar Jha

# ABSTRACT

Solid electrolyte is very important part of the solid oxide fuel cell (SOFC). Currently the yttria stabilized zirconia is being used as an electrolyte material in SOFCs due to it's high ionic conductivity. However, its ionic conductivity decreases drastically below temperature of $1000^{o}C$. Due to this reason, the researchers are concentrating on new materials which could possess high conductivity at low temperature. On the other hand, $ZrO_2$ exhibit monoclinic structure which is stable from room temperature up to $1170^{o}C$ only. The motivation of the present study was to stabilize high temperature $ZrO_2$ cubic (high ionic conductivity) phase at low temperature by doping with $Bi_2O_3$. Various samples synthesized with composition of $ZrO_2$ doped with $Bi_2O_3$ exhibits XRD pattern consisting of three main phase's viz. $Bi_2O_3$, $ZrO_2$ and $Bi_{1.85}Zr_{0.15}O_{3.075.}$ The electrical conductivity as well as thermal study of three samples with composition (15 mol% $Bi_2O_3$ with 85 mol% $ZrO_{2,}$ 20 mol% $Bi_{2}O_3$ with 80 mol% $ZrO_2$ and 25 mol% $Bi_2O_3$ with 75mol% $ZrO_2$ ) was measured and change of one order of conductivity was observed in sample III due to higher disordering present in the sample. Moreover, the structural features of sample III comes out to be different from sample I and sample II. This variation arises due to the liberation of $Bi_2O_3$ phase from inner core of the sample which causes different structural features. Thus it can be concluded that $ZrO_2$ cubic phase could not be stabilized at room temperature after doping with $Bi_2O_3$. The details of the study are presented in subsequent chapters.

## *INDEX*

**CONTENTS** **PAGE NUMBER**

**CHAPTER–4**

**EXPERIMENTAL PROCEDURE**



## CHAPTER-5

**RESULTS AND DISCUSSION**

# CHAPTER – 1 *INTRODUCTION*

## 1.1 Introduction

Fuel cells are electrochemical devices that convert chemical energy into electrical energy directly. They possess high promising power generation with efficiency and low environmental impact. They convert hydrogen, or most hydrogen-containing fuels, directly into electrical energy plus heat through the exothermic electrochemical reaction of hydrogen and oxygen into water. There higher conversion efficiencies, clean operation with low environmental pollution, flexibility of variety fuel used, and relatively noiseless working are among the major advantages over conventional fossil- fuel heat engines [1].

## 1.2 The Discovery of Fuel Cell

The fuel cell was discovered by German Scientist Christian Friedrich Schonbein in 1838 and his finding was published in 1839. First fuel cell was fabricated by William Robert Grove (1839) in which electric current was produced directly from the hydrogen and oxygen. Grove observed that when the current was switched off, a small current flowed through the circuit in the opposite direction, as a result of a reaction between the electrolysis products, hydrogen and oxygen, catalyzed by the platinum electrode. Ceramic fuel cells came into existence much later and began with Nernst's discovery of solid oxide electrolytes in 1899 and the operation of the first ceramic fuel cell at a temperature of 1000°C was demonstrated by Baurand Priesin 1937. In their experiment they used zirconium, yttrium, cerium, lanthanum and tungsten as electrolytes. Much of the research, however, was short lived as melting, short circuiting, and high electrical resistance inside the cell materials created numerous technical hurdles. Their designs were not as good to provide electrical conductivity up to the mark as was expected due to unwanted chemical reactions between the electrolytes and various gases, including carbon monoxide. Thompson also developed a similar fuel cell and reported scaling limitations. This essentially

addressed the difficulty in avoiding leakage of gasses from one chamber to another, as well as various other causes that prevented the E.M.F. of a battery of *n* doubly-coated plates from reaching the conceptually attainable value of *n* times the E.M.F. from a single cell. French researcher Louis Paul Cailleteton and Louis Joseph Colardeau determined that only precious metals would work in a Grove cell. In another development, William W. Jacques, invented the "carbon battery" by injecting air into an alkali electrolyte to react electrochemically with a carbon electrode to produce electricity. [1]

## 1.3 Types of Fuel Cells

There are eight primary classes of fuel cells, identified by their electrolytes which have emerged as viable systems. The electrolyte is a substance used between the anode and cathode, serving as a bridge for the ion exchange that generates electric current. These eight fuel cells are described below:

(i) Polymer Electrolyte Membrane Fuel Cell (PEMFC)

(ii) Alkaline Fuel Cell (AFC)

(iii) Phosphoric Acid Fuel Cell (PAFC)

(iv) Molten Carbonate Fuel Cell (MCFC)

(v) Direct Methanol Fuel Cell (DMFC)

(vi) Solid Oxide Fuel Cell (SOFC)

(vii) Regenerative (Reversible) Fuel Cells **(**RFC**)**

(viii) Zinc-Air Fuel Cells (ZAFC)

### 1.3.1 Proton Exchange Membrane Fuel Cell (PEMFC)

The proton exchange membrane fuel cell or PEMFC is one of the most promising fuel cell types for widespread use because of high power density, light weight and volume, and low operating temperature. PEM fuel cells use a solid polymer (generally Nafion) as an electrolyte and porous carbon electrodes containing a platinum catalyst. The platinum catalyst chemically activates the reactions at the electrodes.

Recent development in manufacturing techniques and processes allows the use of extremely thin layer of platinum, thereby substantially reducing material cost. Hydrogen, oxygen from the air, and water are the fluids required to operate PEMFCs, unlike the corrosive fluids needed in some other fuel cells. As such they are primarily being considered for transportation applications along with some stationary applications. Due to their fast start-up time, low sensitivity to orientation, and favourable power-to-weight ratio, PEM fuel cells are perhaps the most attractive candidates for alternative "engines" in passenger vehicles, such as cars and buses. Polymer electrolyte membrane (PEM) fuel cells also called proton exchange membrane fuel cells deliver high power density and offer the advantages of low weight and volume, compared to their fuel cells [2,3] . However, the combination of Platinum/Ruthenium in the electro catalyst, improves the tolerance.

### 1.3.2 Alkaline Fuel Cell (AFC)

These cells can achieve power generating efficiencies of up to 70 %. They were used on the Apollo spacecraft to provide both electricity and drinking water [2]. Their operating temperature is between 150 to 200°C. The big advantages of this system are its very short start up time, less use of expensive materials and high efficiencies compared to the other fuel cell types [3]. Until recently they were too costly for commercial applications. They typically have a cell output from 300 watts to 5kW. AFCs' have high performance. They have also demonstrated efficiencies near 60% in space applications. The main disadvantage of the AFC is probably its sensitivity of the potassium hydroxide to $CO_2$ poisoning and of the catalyst to CO poisoning [3].

### 1.3.3 Phosphoric Acid Fuel Cell (PAFC)

Phosphoric acid fuel cells use liquid phosphoric acid as an electrolyte the acid is contained in Teflon bonded silicon carbide matrix and porous carbon electrodes containing a platinum catalyst [2]. The phosphoric acid fuel cell (PAFC) is considered the" first generation" of modern fuel cells. It is one of the most mature cell and the first to be used commercially. This type of fuel cell is typically used for stationary power generation, but some PAFCs have been used to power large vehicles such as city buses. One of the main advantages to this type of fuel cell is that it can use impure hydrogen as fuel.

The main disadvantage of PAFC fuel cell is that it uses expensive platinum as a catalyst at the same time it generates low current and it generally has a large size and weight.

### 1.3.4 Molten Carbonate Fuel Cell (MCFC)

Molten Carbonate fuel cells (MCFC) use high temperature compounds of salt (like sodium or magnesium) carbonates (chemically, $CO_3^{2-}$ as the electrolyte) . Efficiency ranges from 60 to 80 percent and operating temperature is about 650°C [2, 3]. The high operating temperature serves as a big advantage because this implies higher efficiency and the flexibility to use more types of fuels and inexpensive catalysts as the reactions involving breaking of carbon bonds in larger hydrocarbon fuels occur much faster as the temperature is increased.

A disadvantage to this, however, is that high temperatures enhance corrosion, the breakdown of cell components and slow start up times. When heated to a temperature of around 650ºC, these salts melt and become conductive to carbonate ions ($CO_3^{2-}$). These ions flow from the cathode to the anode where they combine with hydrogen to give water, carbon dioxide and electrons. These electrons are routed through an external circuit back to the cathode, generating electricity and by-product heat.

### 1.3.5 Direct Methanol Fuel Cells (DMFC)

Most fuel cells are powered by hydrogen, which can be fed to the fuel cell system directly or can be generated within the fuel cell system by reforming hydrogen rich fuels such as methanol, ethanol, and hydrocarbon fuels [2, 3]. Direct methanol fuel cells (DMFCs), however, are powered by pure methanol, which is mixed with steam and fed directly to the fuel cell anode. Methanol undergoes electrochemical reaction with water to $CO_2$ at an operating temperature of 80 to130°C.This low temperature makes short start up time possible. Efficiencies of about 40% are expected with this type of fuel cell, which would typically operate at a temperature between 50 to 100°C. This is a relatively low range, making this fuel cell attractive for small to medium sized applications, to power cellular phones and laptops. Higher efficiencies are achieved at higher temperatures A major problem, however, is fuel crossing over from the anode to the cathode without producing electricity. Other drawbacks of the DMFC are the excessive use of expensive materials like platinum (up to ten times more than high performance PEMFCs) and ruthenium, and the toxicity of $CH_3OH$. Low cell voltage, resulting in low current density, is caused by crossover of neutral methanol from anode to cathode side.

### 1.3.6 Solid Oxide Fuel Cell (SOFC)

Solid oxide fuel cells are the most efficient devices yet invented for conversion of chemical fuels directly into electrical power. Considerable advances in theory and experiments are still being made over after 100 years of invention of its basic idea and materials by Nernst and his colleagues. On the molecular scale, collisions between hydrogen and oxygen molecules result in producing water and releasing heat where as the bond energy of the produced water is lower than the bonding configuration of the initial hydrogen and oxygen gases.

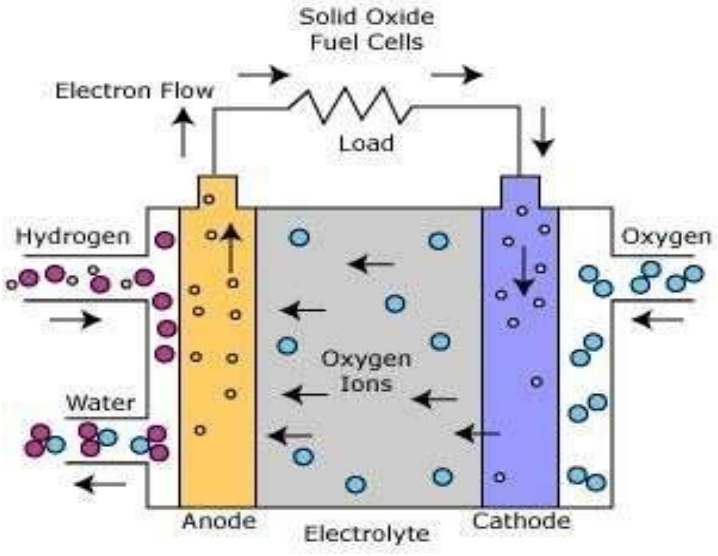


Fig.1.1 working of solid oxide fuel cell

This energy difference is released as heat for combustion engines which occurs by reconfiguration of electrons in Pico seconds at an intimate, sub atomic scale. To produce electricity, this heat energy must be converted into mechanical energy and then the mechanical energy must be converted into electrical energy which is potentially complex and in efficient.

SOFCs use a pre-fabricated hard, non- porous ceramic compound as the electrolyte, sandwich between electrodes. The electrolyte can be manufactured in variety of geometries: tubular, plate or planar, corrugated plate, etc. SOFCs operate at relatively high temperatures around 1000°C, and are expected to around 50-60 % efficient at converting fuel to electricity. It also allows internal fuel reforming, which enables the user operation of a variety of hydrocarbons as fuels and reduces the cost associated with adding a reformer to the system. They are the most sulphur-resistant fuel cell type, can tolerate several orders of magnitude more sulphur than others, SOFCs are not poisoned by carbon monoxide (CO), which can even be as used fuel. This allows us to use gases made from coal. High temperature exit gases making them an ideal candidate for combined heat and power generation (CHP or co-generation) system.

High-temperature operation, however, has some disadvantages. It results in a slow start up and requires significant thermal shielding so as to retain heat and protect personnel, which may be acceptable for utility applications but not for transportation and small portable applications. The high operating temperatures also place stringent durability requirements on materials, and the development of low-cost materials with high durability is a key technical challenge facing this technology. The current research emphasis is on exploring the potential for developing lower-temperature SOFCs operating at or below 800ºC that have fewer durability problems and also cost less. The electrons travel an external circuit providing electric power and producing by-product heat.

Anode Reaction: $2\ H_2 + 2\ O^{2-} \Rightarrow 2\ H_2O + 4\ e^-$ .....(1)

Cathode Reaction: $O_2 + 4\ e^- \Rightarrow 2\ O^{2-}$ .....(2)

Overall Cell Reaction: $2\ H_2 + O_2 \Rightarrow 2\ H_2O$.....(3)

## 1.3.6 (I) Components of SOFC

In order for SOFCs to reach their commercial potential, the materials and processing must also be cost-effective. The first successful SOFC used platinum as both the cathode and anode, but fortunately less expensive alternatives are available today. There are five types of components which are discussed below:

### (a) Cathode

The cathode must meet all the above requirements and be porous in order to allow oxygen molecules to reach the electrode/electrolyte interface. In some designs (e.g. tubular) the cathode

contributes over 90% of the cell's weight and therefore provides structural support for the cell. Presently the most commonly used cathode material is lanthanum magnetite ($LaMnO_3$), a p-type perovskite. Typically, it is doped with rare earth elements (eg. Sr, Ce, Pr) to enhance its conductivity. Most often it is doped with strontium and referred to as LSM ($La_{1-x}Sr_xMnO_3$). The conductivity of these perovskites is all electronic (no ionic conductivity). Any reduction in operating temperature reduces operating costs and expands the materials selection, creating an opportunity for additional cost savings [4].

## (b) Electrolyte

When the molecular oxygen has been converted to oxygen ions it must migrate through the electrolyte to the fuel side of the cell. For such migration to occur, the electrolyte must possess a high ionic conductivity and no electrical conductivity. It must be fully dense to prevent short circuiting of reacting gases through it and it should also be as thin as possible to minimize resistive losses in the cell. As with the other materials, it must be chemically, thermally, and structurally stable across a wide temperature range. YSZ is the most suitable electrolyte material. Yttria serves the dual purpose of stabilizing zirconia into the cubic structure at high temperatures and also providing oxygen vacancies at the rate of one vacancy per mole of dopant. Bismuth oxide-based materials have a high oxygen ion conductivity and lower operating temperature (less than 800°C) , but do not offer enough crystalline stability at high temperature to be broadly useful. Alternative electrolyte deposition methods are spray coating and dip coating followed by sintering. Colloidal suspensions of YSZ are applied in thin layers of at least 20 microns, using nano size (5-10 nm) particles in order to meet the critical requirement of low porosity. Through careful engineering of the particle size distribution and dispersions, these deposition methods are likely to replace electrochemical deposition. Cerium oxide has also been considered as a possible electrolyte.

Its advantage is that it has high ionic conductivity in air but can operate effectively at much lower temperatures (under 700°C); this temperature range significantly broadens the choice of materials for the other components, which can be made less expensive and more readily available materials. But the problem is that this electrolyte is susceptible to reduction on the anode (fuel) side. At low operating temperatures (500-700°C) grain boundary resistance is a significant to ionic conductivity [4].

## (c) Anode

The anode (the fuel electrode) must meet most of the same requirements as the cathode for electrical conductivity, thermal expansion compatibility porosity, and must function in a reducing atmosphere. The reducing conditions combined with electrical conductivity requirements make metals good. Anodes are applied to the fuel cell through powder technology processes [4].

Either slurry of Ni is applied over the cell and then YSZ is deposited by electrochemical vapor deposition, or Ni-YSZ slurry is applied and sintered. More recently NiO-YSZ slurries have been used, the NiO being reduced to particulate Ni in the firing process. In order to maintain porosity, pore formers such as starch, carbon, or thermosetting resins are added. These burn out during firing and leave pores behind. Recent research is investigating the possibility of a freeze-drying approach to forming porous structures without the use of fillers. The slurry is applied through a simple dipping process and then freeze-dried. The resulting ice is then sublimed out of the unfired structure. The resulting pore structure is neatly aligned because of the crystallization of water which allows efficient flow of gases to and from the electrolyte/anode interface. Cu-cerium oxide anodes are being studied as a possible alternative. Copper is an excellent electrical conductor but a poor catalyst of hydrocarbons; cerium oxide is used as the matrix in part because

of its high activity of hydrocarbon oxidation. A composite of the two thus has the advantage of being compatible with cerium oxide electrolyte fuel cells [4].

### (d) Interconnect

The high operating temperature of the cells combined with the severe environments means that interconnects must meet the most stringent requirements of all the cell components: 100% electrical conductivity, no porosity (to avoid mixing of fuel and oxygen), thermal expansion compatibility, and inertness with respect to the other fuel cell components. It will be exposed simultaneously to the reducing environment of the anode and the oxidizing atmosphere of the cathode. For a YSZ SOFC operating temperature is about 1000°C. The material which can be used as interconnect is LaCrO3 doped with a rare earth element (Ca, Mg, Sr, etc.) to improve its conductivity. Ca-doped yttrium chromites are also being considered because it has better thermal expansion compatibility, especially in reducing atmospheres. Interconnects are applied to the anode by plasma spraying and then the entire cell is co-fired. At operating temperatures in the 900-1000°C range, interconnects made of such nickel base alloys as Inconel 600°C are possible. At or below 800°C, ferrite steels can be used. At even lower temperatures (below 700°C), it becomes possible to use stainless steels, which are comparatively inexpensive and readily available [4].

## 1.3.7 Regenerative (Reversible) Fuel Cells

The Regenerative Fuel Cell (RFC) is a system that can operate in a closed loop and could serve as the basis of a hydrogen economy operating on renewable energy. Fuel cells generating electricity, heat, and water from hydrogen and oxygen would be used throughout the economically, powering factories, vehicles, and houses. The hydrogen would be generated from the electrolysis of water, splitting it into its constituent components of hydrogen and oxygen, using renewable energy sources such as wind, solar, or geothermal.

Such a system would not require any specific type of fuel cell, but would need an infrastructure to deliver hydrogen to the many fuel cells in use. However, the infrastructure for hydrogen delivery does not exist.

Currently, there is a project led by NASA to develop an efficient and light weight regenerative fuel cell system for use on board an airplane called the Helios that can fly at altitudes near 100,000 feet. The predecessor aircraft was powered by photovoltaic solar cells. The goal is to incorporate both photovoltaic solar cells and a regenerative fuel cell on board.

### 1.3.8 Zinc-Air Fuel Cells (ZAFC)

Zinc-Air Fuel Cells (ZAFCs) share characteristics with a number of the other types of fuel cells as well as some characteristics of batteries. The electrolyte for a ZAFC is a ceramic solid that employs the hydroxyl ion, $OH^-$, as the charge carrier. To achieve the high electrical fuel efficiency with hydrocarbon fuels and high electrolyte conductivity for the charge carrier, the ZAFC operates at 700ºC. The anode is composed of zinc and is supplied with hydrogen or even hydrocarbons. The cathode is separated from the air supply with a gas diffusion electrode (GDE), a permeable membrane that allows atmospheric oxygen to pass through. At the cathode, the oxygen reacts with hydrogen to form hydroxyl ions and water. The high operating temperature of the ZAFC enables internal reforming of hydrocarbons, eliminating the need for an external reformer to generate hydrogen. An additional advantage of the high operating temperature is that the by-product heat can be used to generate high-pressure steam that is useful in many industrial and commercial applications. The electrolyte for the ZAFC has some advantages over other electrolytes. It does not require water saturation as does the polymer membrane of the PEMFC and therefore, cannot dry out, eliminating the need to carefully monitor and control anode and cathode moisture levels. Additionally, as a solid, no leakage of

the electrolyte will occur as can with liquid electrolytes. Due to the consumption of the zinc anode, this component requires replacing at intervals.

### 1.3.6 (II) Properties of SOFC

Solid oxide fuel cells (SOFC) provide a clean, low pollution technology to generate electricity at high efficiencies electrochemically. These fuel cells provide many advantages over traditional energy conversion systems including high efficiency, reliability, modularity, fuel adaptability, quiet, and vibration- free operation of SOFCs. At the temperature ranges of 900 to 1000ºC. In addition to the capability of internally reforming hydrocarbon fuels. These high temperature SOFCs provide high quality exhaust heat for co generation. Solid-oxide fuel cells can directly use hydrocarbon or hydrocarbon-derived fuels. Conversion efficiencies can be considerably greater than those of heat engines, with hybrid cycles in combination with heat engines and its co-generation promising conversion efficiencies is as high as 70% [5]. Among the initially developed devices, the widely used the low temperature phosphoric acid fuel cells [6] and those based on aqueous alkaline electrolytes [7]. However, the aqueous electrolytes may flood the porous electrodes, evaporate, undergo compositional changes, decompose and eventually lead to poor performance. High temperature fuel cells are MCFC and SOFCs. Their working temperature is above $700^0$C. Another advantage of SOFC over the MCFC is that there is a problem of electrolyte migration in MCFC while no such problem exists in the SOFCs. Further the kinetics of present day SOFCs are faster than their molten carbonate counterparts. Solid oxide fuel cells have a wide variety of applications from use as auxiliary power units in vehicles to stationary power generation with outputs from 100 W to 2 MW. Theoretical efficiency of a SOFC device can reach up to 60 %. The higher operating temperature make SOFCs suitable candidates for application with heat engine energy recovery devices or combined heat and power, which further increases overall fuel efficiency.

## 1.4 Various Types of Electrolytes and Their Properties

| Compound → / Properties ↓ | $Al_2O_3$ | $Bi_2O_3$ | $ZrO_2$ | $La_2O_3$ | $B_2O_3$ | $Y_2O_3$ | $Li_2O$ |
|---|---|---|---|---|---|---|---|
| Systematic Name | Aluminium oxide | Bismuth trioxide | Zirconium Oxide | Lanthanum(III Oxide) | Boron trioxide | Yttrium oxide | Lithium Oxide |
| Ionic Radii(Å) | 0.57 | 1.2 | 0.87 | 1.22 | 0.25 | 1.32 | 0.68 |
| Melting Point($^0$C) | 2054 | 824 | 2700 | 2315 | 450 | 2410 | 1200 |
| Boiling Point($^0$C) | 3000 | 1890 | 5000 | 4200 | 1860 | 4300 | 1700 |
| Crystal Structure | Cubic | Monoclinic (at room temp.) | Monoclinic at room Temp. | Hexagonal and cubic | Tri-cordinated at 1 atm | Cubic | Ant fluorite (Cubic) |
| Geometry | Octahedron | Pseudo-Octahedral | Cubic | pentagonal bipyramidal | Trigonal | Octahedral | Tetrahedral ($Li^+$); cubic ($O^{2-}$) |
| Density (g/cm³) | 3.95-4.1 | 8.9 | 5.68 | 6.51 | 2.64 | 5.01 | 2.013 |
| Molar Mass (g/mol) | 101.97 | 465.96 | 123.22 | 325.81 | 69.62 | 225.81 | 45.88 |
| Appearance | Yellow powder | Yellowish | Silvery White | White powder | White Glassy solid | White powder | White powder |
| Valency | III+ | III+ | IV+ | III+ | III+ | III+ | I+ |
| Solubility In water | Insoluble | Insoluble In cold water | Insoluble | Insoluble | 2.2g/100 ml | Insoluble | 6.67at 0.0$^0$C |

## 1.6 Bismuth oxide ($Bi_2O_3$)

Bismuth Oxide exhibits high oxide ion conductivity and can be used as electrolyte material for solid oxide fuel cells. [8]. Bismuth oxide has four polymorphic forms: room temperature stable phase α (monoclinic), metastable β (tetragonal) and γ (BCC), and high temperature δ (FCC) phase.

## 1.7 Phase transition in $Bi_2O_3$

The transitions among the stoichiometric phases of $Bi_2O_3$ are shown in Figure 1.2. At 730°C, the low temperature α (monoclinic) form is transformed to the face centred cubic structure. The cubic structure melts at 825°C. Considerable super cooling of the cubic form into the range of the thermodynamically stable α phase is observed depending upon the thermal history of the sample. Under some conditions, the super cooled cubic form is transformed into the metastable tetragonal phase at 650°C, followed by a transformation to the stable α form between 450 and 550°C. The metastable bcc form (γ) is also observed under some conditions. The bcc phase (γ) appears at just below the temperature for the formation of the tetragonal phase (β). The tetragonal phase (β) lies between the BCC phase (γ) and the FCC phase (δ) for temperatures below 600°C. The bcc phase is obtained by controlled cooling of tetragonal phase (β), and this is another polymorph for which there is some disagreement. The structure of unit cell of α, β, and δ is shown in Figure 1.3, 1.4, and 1.5 respectively. In the case of (δ-$Bi_2O_3$) the black spot is of Bi and white spot is of oxygen.[9]. The measurements demonstrated that the pressure between 0.5 and 2.5 GPa has a significant effect on the $\alpha$–$\delta$ phase transition temperature in $Bi_2O_3$, and the increase of $T_c$ for the $\alpha$–$\delta$ phase transformation is more than $60^0$C compared to previous research with DTA. During cooling, the $\delta$–$\alpha$ transformation occurred approximately at the temperature corresponding to $T_c$ monitored during the heating cycle.

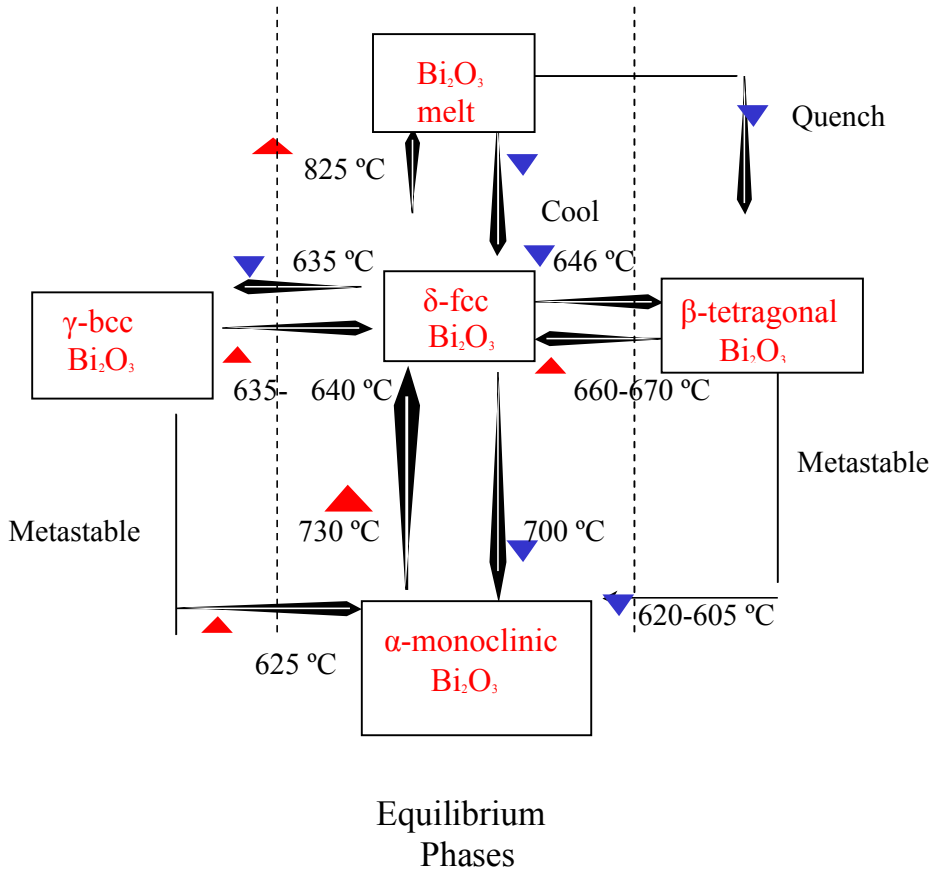


Figure 1.2 Phase transitions of bismuth oxide [9]. Phase transitions in bismuth Oxides are dependent on thermal history and impurities.

Neither a *δ–β*, a *δ–γ* phase transformation nor a hysteresis effect has been found under pressure, which is in contrast with normal pressure studies that used DTA, electrical conductivity measurements and XRD, Polymorphism of Bismuth Sesquioxid.

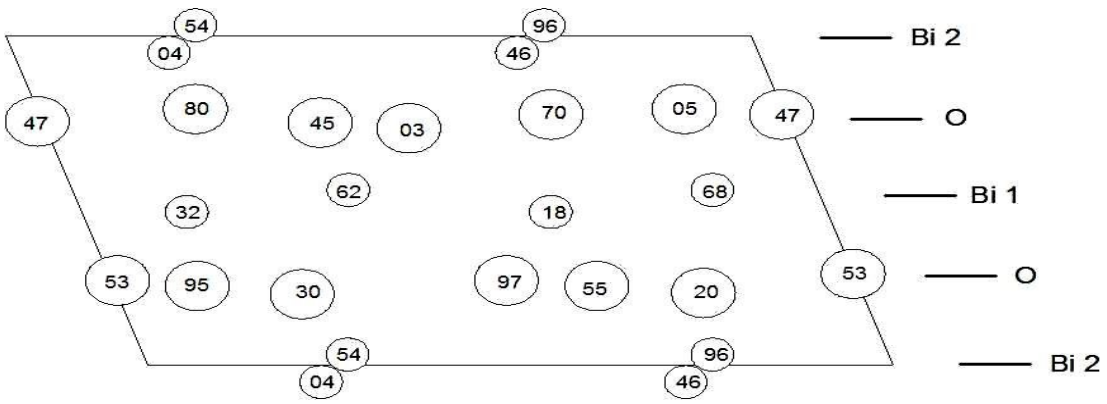


Figure 1.3 Projection of the α-$Bi_2O_3$ structure on the (010) plane. The position parameters in the <010> directions are multiplied by 100 [10].

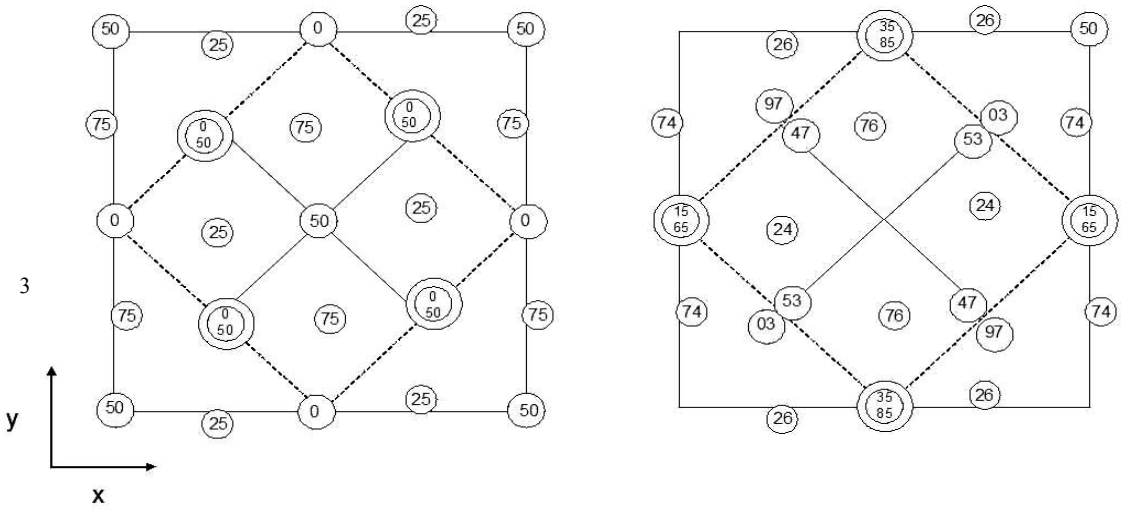


Figure 1.4 Projection of the β-Bi2O3 structure on the (001) plane. The oxygen cubes in the Fluorite structures are indicated. The position parameters in the <001> direction are multiplied by 100 [10].

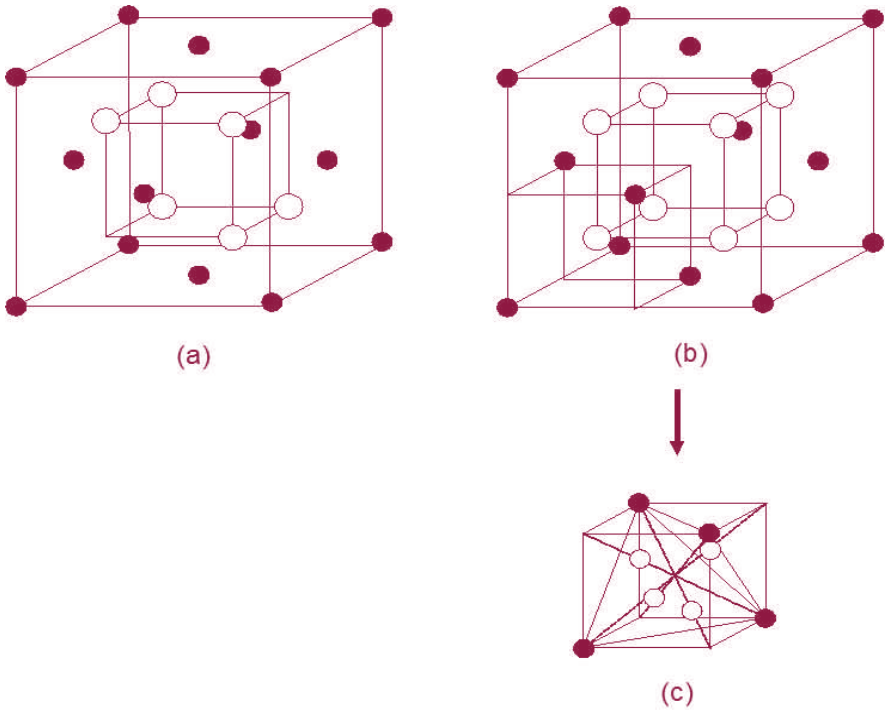


Figure 1.5. Fluorite related structure model for δ-$Bi_2O_3$: (a) Sillen model, (b) Gattow model and (c) Willis model [10].

## 1.8 Zirconium Oxide ($ZrO_2$)

Zirconia is an extremely hard refractory material. It offers chemical and corrosion inertness to temperatures well above the melting point of alumina. The material has low thermal conductivity. It is electrically conductive above 600°C and is used in oxygen sensor cells and as the susceptor (heater) in high temperature induction furnaces. With the attachment of platinum leads, can be made as a light emitting filament which operates in air. Pure zirconia exists in three crystal phases at different temperatures.

At very high temperatures (>2370°C) the material has a cubic structure. At intermediate temperatures (1170 to 2370°C) it has a tetragonal structure. At low temperatures (below 1170°C) the material transforms to the monoclinic structure. The transformation from tetragonal to monoclinic is rapid and is accompanied by 3 to 5 percent volume increase that causes extensive cracking in the material. This behaviour destroys the mechanical properties of fabricated

components during cooling and makes pure zirconia useless for any structural or mechanical application. The transformation in zirconia crystal structure can be slowed down or eliminated by suitable dopants. Commonly used effective additives are MgO, CaO, and $Y_2O_3$. With sufficient amounts added, the high temperature cubic structure can be maintained to room temperature. Cubic stabilized zirconia is a useful refractory and technical ceramic material because it does not go through destructive phase transitions during heating and cooling. The controlled, stress induced volume expansion of the tetragonal to monoclinic inversion is used to produce hard, high strength, and tough Varity of zirconia suitable for mechanical and structural applications. There are several different mechanisms that lead to strengthening and toughness in zirconia that contain tetragonal grains. In general, these depend on the grain sizes, the thermal history and the kind and amount of stabilizing additive in the body. These variations lead to two strong, commercially available partially stabilized zirconia (PSZ) microstructures identified as TTZ (tetragonally toughened zirconia) and TZP (tetragonal zirconia polycrystalline) ceramics. The TTZ is an MgO partially stabilized zirconia often designated MgTTZ or MgPSZ consisting of uniformly dispersed tetragonal precipitates in larger cubic phase crystals. The secondary thermal aging process requiring tight manufacturing controls for proper microstructural development to get tetragonally toughened zirconia has limited because of complication in processing. The second variety, TZP, is a pure tetragonal phase, very fine grain material stabilized with rare earth oxides, primarily yttria and less commonly ceria. They are often designated as YTZP for the yttria stabilized product and CeTZP for the ceria stabilized product.

The TZP material has found uses in cutting and wear resistant applications due to its reliable and outstanding hardness and toughness. TZP properties degrade rapidly when the material is exposed to water vapour at 200 to 300°C, so controlled use conditions are important for good performance. All of the toughened zirconias show a degrading of properties with increasing temperature, and this class of high strength, tough materials is generally limited to use

temperatures below 800°C. In figure 1.6 (a) the black spot is of Zr and brown colour is of oxygen [11]

.

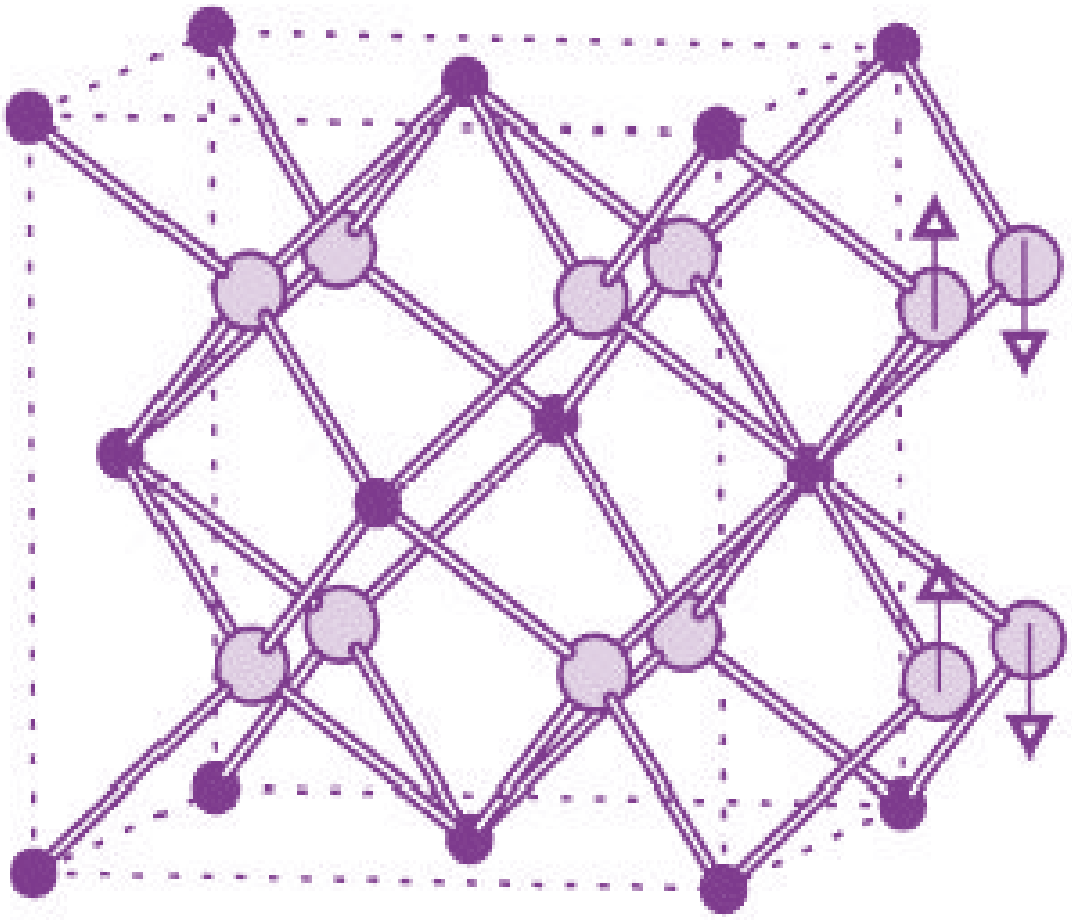

**(a)**

Figure 1.6. (a) Atomic positions for cubic and tetragonal form [11].

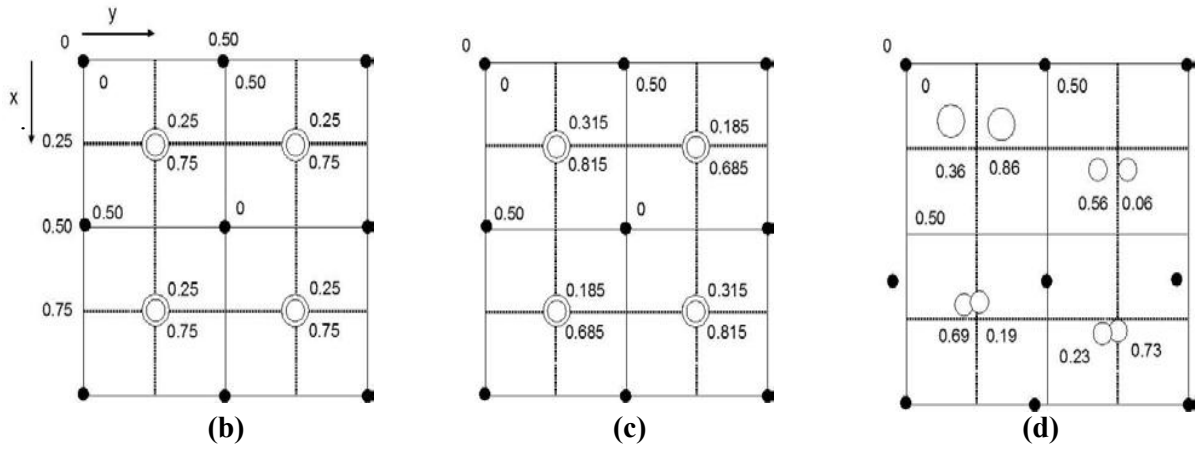


Figure 1.7. Projection of $ZrO_2$ structures (b) cubic (fluorite) form, (c) tetragonal form and (d) monoclinic form [12].

## 1.9. $Bi_2O_3$-$ZrO_2$ System

Phase diagram is available only for the $Bi_2O_3$-rich end (see Figure 1.8). Even at this end, the locations of phase boundaries are not firmly established (shown by dashed curves in Figure 1.8). Tetragonal β-$Bi_2O_3$ can be stabilized by adding $ZrO_2$ [13]. Figure 1.8 shows a -rich part of $Bi_2O_3$-$ZrO_2$ binary system. In 1964, a study $Bi_2O_3$ by Hund [14] suggested an extensive solid solution range from 0 to 70 mole% $ZrO_2$ that possesses the tetragonal structure of β-$Bi_2O_3$. It was reported that at 60 mole% $ZrO_2$, the structure consists of an ideally filled anion lattice with interstitial cations, whereas pure β-$Bi_2O_3$ has an ideally occupied cations sub lattice with vacancies in the anion sub lattice. More recently an investigation by Sorokin's and Sleight [15] on the $Bi_2O_3$-$ZrO_2$ binary system indicated that a defect fluorite solid solution exists in the range of 40-66 mole% $ZrO_2$, when samples were calcined at 600°C. The reported range of the solid solution decreases with increasing temperature of the calcinations until temperatures above 750°C. Only the equilibrium phases $ZrO_2$ and $Bi_{1.84}Zr_{0.16}O_{3.08}$ are stabilized. This latter phase was reported to possess a β-$Bi_2O_3$ structure.

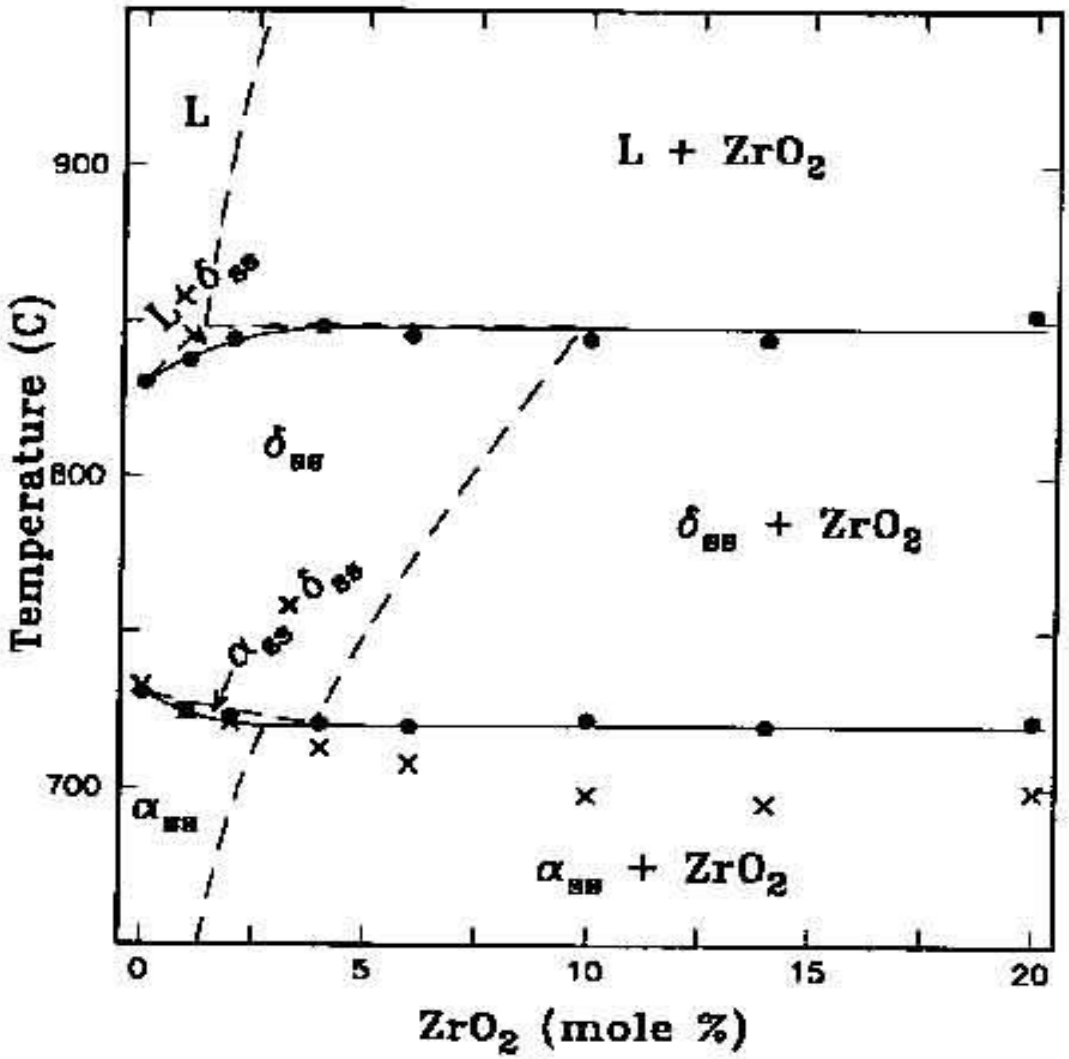


Figure 1.8. Binary phase diagram of $Bi_2O_3$ and $ZrO_2$ at low $ZrO_2$ contents [15].

# CHAPTER – 2 *LITERATURE REVIEW*

Solid electrolytes are materials which find their application in several devices like electrochemical cells, sensors etc. The basic property which is responsible for the development of such technology is the ionic conductivity of the material. In order to improve the ionic conductivity to have a technical product of better performance, researchers are trying hard to synthesize new compounds exhibiting higher ionic conductivity. The requirement of new product where oxide ion conductivity plays dominant role such as SOFC is increasing to save the fuel, a conventional source of energy [16]. The present challenges for the commercialization of planar solid oxide fuel cell is the reduction of its operating temperature, which requires the optimization of the electrolyte nature and ionic conductivity. Thin layer technology seems suitable to decrease the electrolyte resistance at lower operating temperatures. In the recent past, various types of solid electrolyte materials which have been studied are $ZrO_2$-based, $ThO_2$-based, $CeO_2$-based, $HfO_2$-based [17-18], and $Bi_2O_3$-based electrolytes [19-20]. The cations sub lattice causes the formation of anion vacancies to preserve electrical neutrality. This results in the increase of ionic conductivity of oxide electrolyte through the conduction of $O^{2-}$ ions under certain conditions of temperature and pressure [18].

Yttria stabilized zirconia (YSZ) is the most common material which have been used as a solid electrolyte in SOFC. YSZ exhibits adequate ionic conductivity in reducing and oxidizing atmosphere. The ionic conductivity of stabilized zirconia is independent of oxygen partial pressure over several orders of magnitude in a wide range of temperature [21,22]. The most commonly used stabilizing oxides or dopants are CaO, MgO, $Sc_2O_3$ and certain rare earth oxides. The conductivity increases as the radius of the dopant cations approach to that of zirconium.

Thus, Scandia doped zirconia shows the highest conductivity ($rSc^{3+}$ = 0.81 Å and $rZr^{4+}$= 0.8 Å). YSZ is the most suitable solid electrolyte in all respect at higher temperature ($1000^{o}C$). However, higher operating temperature (~$1000^{o}C$) causes degradation due to the aging effects in YSZ electrolyte.

Abraham *et. al.* [23] reported the solid state system $Bi_2O_3$:$ZrO_2$ up to 28 mol% $ZrO_2$ using X-ray and neutron powder diffraction, ac impedance spectroscopy and differential thermal analysis. They reported that the solid state solution with general composition $Bi_{2-x}Zr_xO_{3+x/2}$ ($0.05 \leq x \leq 0.17$) adopt a new β-$Bi_2O_3$ type structure termed $\beta_{III}$, which is closely related to $Pb_2F_2O$. DTA and ac impedance measurements indicated a complex phase transition to a highly conducting polymorph ($\sigma_{700}$=1.02 $Scm^{-1}$) at temperature above $690^{0}C$ on heating.

Anderson *et al.* [24] have studied the reactivity of yttria-stabilized zirconia (YSZ) with compounds of the form $Ln_{0.8}Sr_{0.2}FeO_3$ (Ln=Sm, Pr, Nd and a mixed lanthanide precursor) and $La_{0.8}M_{0.2}FeO_3$ (M=Ba, Ca). From this study, the most promising candidate for direct application to YSZ is probably $La_{0.8}Ca_{0.2}FeO_3$ since it indicates decreased dissolution of Zr into the perovskite at 1200°C, and the ability to be sintered from 1000 to 1100°C, potentially avoiding any major interaction with the YSZ.

Zhu and Fan [25] have synthesized 8 mol% yttria doped zirconia (8YSZ) nanocrystals at 200°C, through a hydrothermal process. Characterizations revealed that the as-synthesized 8YSZ powder was weakly agglomerated and had a surface area of $121m^2/g$ and an average grain size of 9 nm. Sintering behaviours of the 8YSZ powder were studied via isothermal and non-isothermal experiments. It demonstrated that the powder has high sintering activity, where 8YSZ green films prepared via dip coating using the slurry directly formed by the hydrothermal process can be fully densified at 1000°C. The thickness of the sintered film can be controlled through adjusting the 8YSZ concentration in the slurry and repeating the dipping–coating–sintering cycle.

The good sinter ability of 8YSZ was mainly attributed to the high green density and homogeneity of the green bodies with narrow-distributed interparticle pore structure. The low sintering temperature is of great practical importance for improving film quality and facilitating co-sintering of 8YSZ films together with other SOFC components.

Jiang *et.al.* [26] developed a $Bi_2O_3$ electrolyte doped with $Dy_2O_3$ and $WO_3$ (DyWSB) that exhibits a higher conductivity than that of 20 mol% ebria stabilized bismuth oxide (20ESB), thus giving it highest conductivity of any known solid oxide electrolyte. The dopants were selected based on their polarizability and its effect on structural stability and conductivity.

Antonino Gulino *et.al.* [27] reported low-temperature (400-800°C) stabilization of tetragonal zirconia using hydroxide gel route and low temperature annealing. A phase transition from the tetragonal structure of zirconia to the monoclinic phase takes place above 800°C.At temperature lower than 500°C the undoped $ZrO_2$ they are amorphous. At 500°C some evidence of crystalline phases are present in terms of monoclinic and less intense tetragonal XRD reflections. At higher firing temperatures the tetragonal lines become weaker and at 800°C samples are completely monoclinic. The Bi- doped samples annealed up to 300°C are amorphous .Above 300°C, broad peaks, corresponding to the formation of crystalline phase, begin to appear. The crystallization is completed at 400°C .In Bi- doped $ZrO_2$ with 7%,10%and 15% bismuth doped they have grain size present are similar to those found for cubic, pure nanocrystalline $ZrO_2$.

The XPS spectra reveal the presence of Bi (III) and of a small amount of a lower Bi oxide. Progressive heating treatment of Bi-doped $ZrO_2$ cause surface segregation of the Bi oxide which separates from the tetragonal phase and giving the thermodynamically more stable monoclinic $ZrO_2$.

S. Tekeli *et.al.* .[28] reported that XRD analysis of the c-$ZrO_2$ specimens containing less than 5 wt% $TiO_2$. It revealed only cubic fluorite reflection, whereas XRD of the specimens with greater than 5 wt% showed the cubic fluorite and tetragonal phase.

$TiO_2$ destabilized cubic zirconia phase caused the formation of tetragonal phase. The lattice parameter of the c-$ZrO_2$ decreased with increasing TiO2 content. The decrease in lattice parameter with increasing TiO2 content in the c-$ZrO_2$ showed that Ti goes into solid solution. The lower values of the lattice parameter found for the $TiO_2$ doped c-$ZrO_2$ could be due to the dissolution in the cubic phase of $TiO_2$ and the substitution of smaller $Ti^{4+}$ ions for $Zr^{4+}$ and $Y^{+3}$ ions in the cubic lattice. Grain size measurements for undoped and $TiO_2$ doped c-$ZrO_2$ specimens sintered at 1450°C showed that grain size decreased with increasing $TiO_2$ content. The grain, grain boundary and total conductivity of c-$ZrO_2$ decreased with increasing $TiO_2$ content. This decrease was due to both a trapping of the oxygen ion vacancies by Ti ions and the formation of tetragonal phase which gives rise to a reduction in moving oxygen vacancies.

Naumovich *et al.* [29] reported the electrical conductivity, oxygen ion transference numbers and thermal expansion of solid solutions Bi $(Zr,Y)O_{1.5}$ and Bi $(Zr, Pr)O_{1.5}$. They concluded that the monoclinic distortion, inherent to the crystal lattice of Zr(Y) O1.5 can be relieved on addition of Bi. A possible explanation is that the radii of ($Bi^{3+}$=1.2 Å, $Zr^{4+}$=0.87 Å, $Y^{3+}$=1.06 Å) Bi cations is much larger than Zr ion. Consequently, addition of $Bi_2O_3$ results in the increase of the lattice parameter in the series of solid solutions. Thermal stability at low temperature requires more detailed investigations so far as worsening of mechanical properties and second phase segregation was observed after long term ( above ten months ) storage of the ceramics at room temperature.

Vanier *et .al.* [30] studied $Bi_4V_2O_{11}$ powdered samples and single crystals by high temperature X-ray diffraction and impedance spectroscopy to characterize the phase transitions From high temperature X-ray diffraction on powders and single crystals, the $\alpha\leftrightarrow\beta$ and $\beta\leftrightarrow\gamma$ reversible phase transitions were observed.

The β↔γ one is ferroelastic ↔ paraelastic but surprisingly the α↔β transition also exhibits a ferroelastic character, with a 90°C switching of the a and b axis on cooling and/or, more scarcely on heating.

Abrahams *et.al.* [31] discussed the defect structure of the BIMEVOX and constructed general defect equations for solid solution formation range. Two limiting models were proposed by which solid solution formation can occur. In the Equatorial vacancy (EV) model, vacancies are located exclusively in the bridging sites in the vanadate layer. In contrast, the Apical Vacancy (AV) model assumes vacancies are located exclusively in non-bridging apical sites in the vanadate layer. The general defect equations can be used to predict theoretical solid solution limits for all types of substitutions for vanadium in $Bi_4V_2O_{11-\delta}$. These limits are found to vary not only with charge of the dopant ion, but also with the coordination number of the metal dopant. In most cases it is found that the EV model yields theoretical solid solution limits close to those observed. The EV model is also used to present a mechanism for ionic conduction in BIMEVOXes, which involves movement of equatorial oxide ions/vacancies between vanadium octahedral and tetrahedral with the formation of five coordinate vanadium intermediate.

Bikramjit Basu *et.al.* [32] reported fully dense tetragonal $ZrO_2$composites with 30 vol.% $TiB_2$ which could be obtained by hot pressing in vacuum at 1450°C for 1 h. The optimum composite has an excellent combination of mechanical properties with a fracture toughness of 10 MPa and a hardness of 13 GPa. The residual tensile stress in the $ZrO_2$ matrix of the $ZrO_2$–$TiB_2$ composites was found to have a significant influence on the transformability of the tetragonal $ZrO_2$ matrix and the overall toughness of the composites. The influence of the residual stress on the transformability was found to be much more pronounced in case of co-precipitated $ZrO_2$ powder based composites when compared to yttria-coated $ZrO_2$ powder based composites. Crack deflection by the $TiB_2$ phase was identified as an active and significant toughening mechanism. While the tetragonal grain size does

not seem to have any influence on the obtained toughness, the yttria distribution in the $ZrO_2$ matrix was identified as an additional variable in controlling the transformability and transformation toughening of the t-$ZrO_2$ phase. This factor coupled with the residual stress in $ZrO_2$ matrix should therefore be considered as design parameters for the future development of the Y-TZP based transformation toughened materials.

Bogicevic *et.al.* [33] calculated the enthalpies for $[(ZrO_2)_{0.90}(Y_2O_3)_{0.10}]$ using exponential fit between temperature range of 400°C to 1000°C, the calculated $\Delta H^a$=0.49eV and $\Delta H_m$=0.68eV.

Yaremchenko *et.al*. [34] concluded that the fluorite-type oxygen-ion conducting solid solutions $(Bi_{1-x}Zr_x)_{0.85}Y_{0.15}O_{1.5+\delta}$ (x = 0.05 and 0.07) and $(Bi_{0.95}Nb_{0.05})_{0.85}Ho_{0.15}O_{1.5+\delta}$ partially decompose at temperatures below 627°C, forming several phases corresponding to structural changes of δ- and γ-$Bi_2O_3$. Formation of the bcc γ- $Bi_2O_3$- -type phases at 497°C leads to a sharp decrease in conductivity. Interaction of the $Bi_2O_3$-based solid electrolytes with silver electrodes was observed at temperatures above 577°C resulting in increasing resistance of the electrochemical cells. Electrodes of platinum and perovskite-type $La_{0.7}Sr_{0.3}CoO_{3-\delta}$ were ascertained to exhibit sufficient stability when in contact with the bismuth oxide-based electrolytes in the temperature range of 597–727°C.

Miodragzdujic *et.al.* .[35] reported that for a nanocrystalline $Bi_{0.78}Hf_{0.59}Zr_{0.63}O_{3.61}$ solid solution with a fluorite-type $Bi_2O_3$ structure which was synthesized by prolonged mechanochemical treatment of a $2Bi_2O_3$+$3HfO_2$ powder mixture in a zirconia medium. The reaction commenced at the very beginning of milling through the formation of a β-$Bi_2O_3$ phase, which grew with the advancement of milling and was finely transformed to a single δ-$Bi_2O_3$ phase. The final phase transition was very likely assisted by the accumulation of $ZrO_2$ arising from the milling tools. Thus, contamination of the milled materials, which in many situations must be judged as undesirable, presents here a favourable process.

According to DSC results, the $Bi_{0.78}Hf_{0.59}Zr_{0.63}O_{3.61}$ solid solution was stable on heating and cooling between room temperature and 900°C. This fact and the relatively high value of the electrical conductivity, close to $0.1Scm^{-1}$ for a temperature of 700°C, make the mechanochemically synthesized $Bi_{0.78}Hf_{0.59}Zr_{0.63}O_{3.61}$ solid solution a promising high oxide ion conductivity material.

Klaartje De Buysser *et.al* [36] concluded that the the thermal expansion of $ZrW_2O_8$ by the formation of composites with $ZrO_2$ has been demonstrated, using two preparation methods. In a Conventional synthetic approach, the variation of the thermal expansion coefficient is shadowed by poor mechanical properties. However, by using an in situ method, there is no loss in flexural strength. The use of polyethylene glycol as pressing aid largely improves the mechanical characteristics of the composite materials. Nevertheless, the formation of pores was observed due to the evaporation of organic material during thermal treatment.

Pernot *et.al*. [37] studied that the partially Cu- or Ni-substituted compounds ($Bi_4V_{2(1-x)}M_{2x}O_{(11-3x)}$; M=Cu, Ni) are highly oxygen conducting. Three phases are observed in the unsubstituted compound; α is the low conducting room temperature phase and γ the high conducting phases at high temperature. Structure and conductivity are studied as a function of substitution on the vanadium sites between 0 and 6% at room temperature, the Cu compound remains in the orthorhombic α phase and its ionic conductivity increases. A strong anisotropic conductivity is also observed.

G. C. T. Silva *et.al*. [38] reported that the addition of Co increases the densification of 8YSZ even for contents as low as 0.05 mol%. The solubility limit for Co in 8YSZ is lower than 5 mol%. In specimens exceeding this limit, $Co_3O_4$ is the preferred formed phase, and no mixed oxide was formed up to 10 mol% Co. The total electrical conductivity decreases with increasing Co content in 8YSZ, whereas the activation energy for conduction decreases, probably due to an increase in the electronic conductivity.

Mingshuai Liu *et.al*. [39] reported that the variation in grain size can produce large change in the activation energy for grain-boundary conduction, $E_{gb}$, and there exists a particular grain size at which $E_{gb}$ reaches a maximum. Based on two existing models, the constriction resistance model and the brick layer model, a possible explanation for this experimental phenomenon was proposed. It was suggested that the possible distribution of grain-boundary phases in a real material may be that along which the path for the migration of oxygen vacancies exists. Here some grain boundaries would keep clean with direct grain-to-grain contact while the others would be filled with a thin precipitate layer. When the grain size is small, the percentage of the clean grain-boundary, i.e. the ratio of the area of the clean grain-boundary to the total grain-boundary area, decreases with increasing grain size, resulting an increasing tendency in $E_{gb}$. When the grain size is large enough, the grain-boundary phases may tend to precipitate at grain-boundary tri-junctions and leave the remaining grain-boundary with direct grain-to-grain contact. As a result, $E_{gb}$ would decrease as grain size increases.

Shu-Ting Kuo *et.al*. [40] reported that the series of chemical reactions take place in the ZnO–$Bi_2O_3$ and ZnO–$Bi_2O_3$–$Sb_2O_3$ specimens during heating and cooling down stages. These reactions can be manipulated by the control of the vaporization of $Bi_2O_3$ and $Sb_2O_3$. The use of the powder bed is a powerful method to reduce the vaporization of $Bi_2O_3$ and $Sb_2O_3$. The presence of the $Bi_2O_3$ rich liquid phase at the boundaries of ZnO grains can deliver uniform microstructure and higher breakdown voltage. The addition of $Sb_2O_3$ into ZnO–$Bi_2O_3$ system induces the formation of inversion boundary and spinel, the microstructure is consequently refined. However, the reaction between spinel and $Bi_2O_3$ to form pyrochlore consumes the liquid phase during the cooling down stage. Lacking the presence of $Bi_2O_3$ rich liquid phase at the grain boundaries, the non-linearity characteristics of the ZnO–$Bi_2O_3$–$Sb_2O_3$ specimens deviate.

The characterization of zirconia based bismuth doped electrolyte has been carried out with various characterization methods. The detail of the techniques used for the investigation is described below:

## 3.1 X-Ray Diffraction Studies (XRD)

X-ray diffraction is the most wide spread technique for the phase identification, crystal structure, lattice parameter of the crystalline solids. A typical powder XRD instrumentation consist of four main components such as X-ray source, specimen stage, receiving optics and X-ray detector as shown in fig.3.1. The source and detector with its associated optics lie on the circumference of focusing circle and the sample stage at the centre of the circle. The angle between the plane of the specimen and the X-ray source is θ, known as Bragg's angle and the angle between the projection of X-ray and the detector is 2θ. For the XRD analysis, fine powder samples were mounted on the sample holder and the powder was assumed to consist of randomly oriented crystallites. When a beam of X-ray is incident on the sample, X-rays are scattered by each atom in the sample. If the scattered beams are in phase, these interfere constructively and one gets the intensity maximum at that particular angle. The atomic planes from where the X-rays are scattered are referred to as 'reflecting planes'.

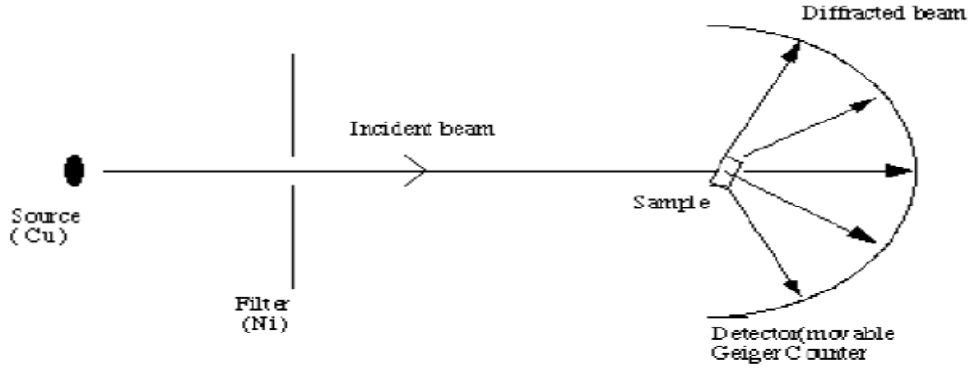


Fig 3.1: X-ray Scattering

The Bragg's law relates the wavelength (λ) of the X-ray reflected the spacing between the atomic planes (d) and the angle of diffraction (θ) as follows:

$$2d \sin \theta = n\lambda$$

For the first order diffraction, n=1, and knowing θ and λ, one can calculate the interplanar spacing d value for a particular plane. After recording the X-ray diffraction pattern, first step involves the indexing of XRD peaks. The indexing means assigning the correct Miller indices to each peak of the diffraction pattern. The correct indexing is done only when all the peaks in the diffraction pattern are accounted for the process. There are three main methods for indexing a diffraction pattern,

(i) Comparing the measured XRD pattern with the standard data base (JCPDS cards)

(ii) Analytical methods

(iii) Graphical methods

In case of fine particles, with reduction in the size of the particles, the XRD lines get broadened, which indicates clearly that particle size has been reduced. Information of the particle size is obtained from the full width at half maximum (FWHMs) of the diffraction peaks. The FWHMs (β) can be expressed as a linear combination of the contributions from the strain (ε) and particle size (L) through the following relation:

$$\text{Cos } \theta/\lambda = 1/L + \varepsilon \text{ Sin } \theta/\lambda$$

## 3.2 Scanning Electron Microscope (SEM)

The scanning electron microscope (SEM) is a type of electron microscope that images the sample surface by scanning it with a high-energy beam of electrons in a raster scan pattern. The electrons interact with the atoms that make up the sample producing signals that contain information about the sample's surface topography, composition and other properties such as

electrical conductivity. The types of signals produced by an SEM include secondary electrons (SE), back scattered electrons (BSE), characteristic x-rays, light (cathodoluminescence), specimen current and transmitted electrons. These signals require specialized detectors that are not usually present on a single machine. The signals result from interactions of the electron beam with atoms at or near the surface of the sample. In the most common or standard detection mode, secondary electron imaging or SEI, the SEM can produce very high-resolution images of a sample surface, revealing details about 1 to 5 nm in size. Due to the way these images are created, SEM micrographs have a very large depth of field yielding a characteristic three-dimensional appearance useful for understanding the surface structure of a sample. A wide range of magnifications is possible, from about X 25 (about equivalent to that of a powerful hand-lens) to about X 250,000, about 250 times the magnification limit of the best light microscopes. Back-scattered electrons (BSE) are beam electrons that are reflected from the sample by elastic scattering. BSE are often used in analytical SEM along with the spectra made from the characteristic X-rays. Because the intensity of the BSE signal is strongly related to the atomic number (Z) of the specimen, BSE images can provide information about the distribution of different elements in the sample. For the same reason, BSE imaging can image colloidal gold immune-labels of 5 or 10 nm diameter which would otherwise be difficult or impossible to detect in secondary electron images in biological specimens. Characteristic X-rays are emitted when the electron beam removes an inner shell electron from the sample, causing a higher energy electron to fill the shell and release energy. These characteristic x-rays are used to identify the composition and measure the abundance of elements in the sample. In a typical SEM, an electron beam is thermionically emitted from an electron gun fitted with a tungsten filament cathode. Tungsten is normally used in thermionic electron guns because it has the highest melting point and lowest vapour pressure of all metals, thereby allowing it to be heated for electron emission and easily available.

Other types of electron emitters include lanthanum hexaboride ($LaB_6$) cathodes, which can be used in a standard tungsten filament SEM if the vacuum system is upgraded and field emission guns (FEG), which may be of the cold-cathode type using tungsten single crystal emitters or the thermally-assisted Schottky type, using emitters of zirconium oxide.

The electron beam, which typically has an energy ranging from a few hundred eV to 40 keV, is focused by one or two condenser lenses to a spot about 0.4 nm to 5 nm in diameter. The beam passes through pairs of scanning coils or pairs of deflector plates in the electron column, typically in the final lens, which deflect the beam in the *x* and *y* axes so that it scans in a raster fashion over a rectangular area of the sample surface. When the primary electron beam interacts with the sample, the electrons lose energy by repeated random scattering and absorption within a tear drop-shaped volume of the specimen known as the interaction volume, which extends from less than 100 nm to around 5 μm into the surface. The size of the interaction volume depends on the electron's landing energy, the atomic number of the specimen and the specimen's density. The energy exchange between the electron beam and the sample results in the reflection of high-energy electrons by elastic scattering emission of secondary electrons by inelastic scattering and the emission of electromagnetic radiation, each of which can be detected by specialized detectors. The beam current absorbed by the specimen can also be detected and used to create images of the distribution of specimen current. Electronic amplifiers of various types are used to amplify the signals which are displayed as variations in brightness on a cathode ray tube. The raster scanning of the CRT display is synchronised with that of the beam on the specimen in the microscope, and the resulting image is therefore a distribution map of the intensity of the signal being emitted from the scanned area of the specimen.

The image may be captured by photography from a high resolution cathode ray tube, but in modern machines is digitally captured and displayed on a computer monitor and saved to a computer's hard disc.

Magnification in a SEM can be controlled over a range of up to 6 orders of magnitude from about X 25 to X 250,000 and exceptionally to 2 million times in the Hitachi S-5500 in-lens Field Emission SEM, imaging a specimen area about 60nm wide with resolution up to 0.4 nm. Unlike optical and transmission electron microscopes, image magnification in the SEM is not a function of the power of the objective lens. SEMs may have condenser and objective lenses, but their function is to focus the beam to a spot, and not to image the specimen. Provided the electron gun can generate a beam with sufficiently small diameter, an SEM could in principle work entirely without condenser or objective lenses, although it might not be very versatile or achieve very high resolution.

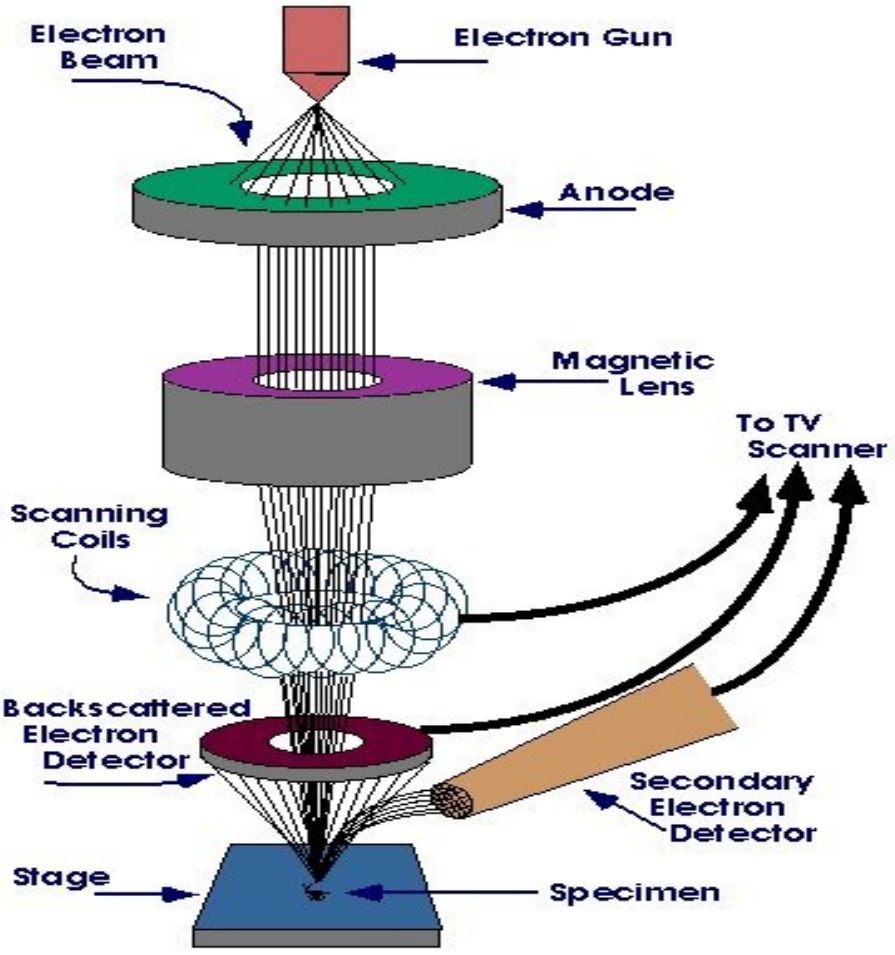


Fig 3.2. Schematic ray diagram of SEM

## 3.3 Conductivity Measurement

A.c. conductivity is one of the studies done on solids in order to characterize the bulk resistance of the crystalline sample. Measurement of a.c. conductivity can be done by different techniques. The currently used technique is the complex impedance spectroscopy. This study also gives information on electrical properties of materials and their interface with electronically conducting electrodes. The complex impedance spectroscopy measurement of a.c. conductivity is based on studies made on the measurement of cell impedance/admittance over a range of temperatures and frequencies and analysing them in complex impedance plane (Bauerle 1969; Macdonald 1987). This is particularly characterized by the measurement and analysis of $Z$ (impedance), $Y$ (admittance) and plotting of these functions in the complex plane which is known as Nyquist diagrams. Impedance is a more general concept than resistance because it takes phase differences into account. In a.c., the resistance, $R$, is replaced by the impedance, $Z$, which is the sum of resistance and reactance. Impedance can be written as

$$Z = Z' + Z'',$$

\

Where $Z'$ is the real part and $Z''$ the imaginary part of $Z$. $Z$ is a vector quantity and may be plotted in the plane with either rectangular or polar coordinates as shown in figure 3.3. The two rectangular coordinate values are

$$\text{Re}\,(Z) = Z' = |Z| \cos \varphi,$$

$$\text{Im}(Z) = Z'' = |Z| \sin \varphi,$$

With phase angle $\varphi = \tan{-1}_{(}Z'/Z'')$ and $|Z| = [(Z')^2 + (Z'')^2]^{1/2}$.

In polar form, $Z$ may be written as

$$Z(\omega) = |Z| \exp(j\omega),$$

Where $\exp(j\omega) = \cos(\varphi) + j \sin(\varphi)$.

In general, *Z* is frequency dependant. Impedance spectroscopy consists of the measurement of *Z* (ω) over a wide frequency range. It is from the resulting structure of *Z* (ω) vs. ω one derives information about the electrical properties of the electrode material system. Impedance plane plots for series and parallel combinations of *R* and *C* are shown in figure 3.4. A symmetrical solid cell system can be represented by the simplified general equivalent circuit as shown in figure3.5.

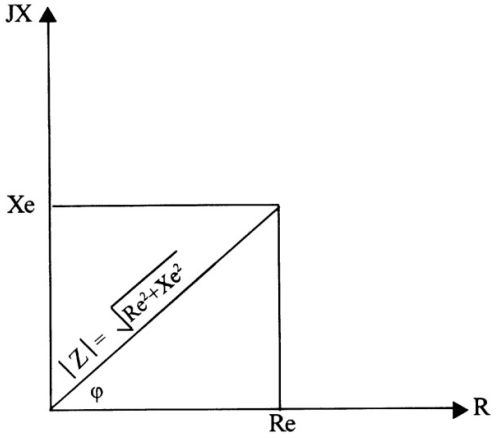


Figure3.3
Impedance vector representation

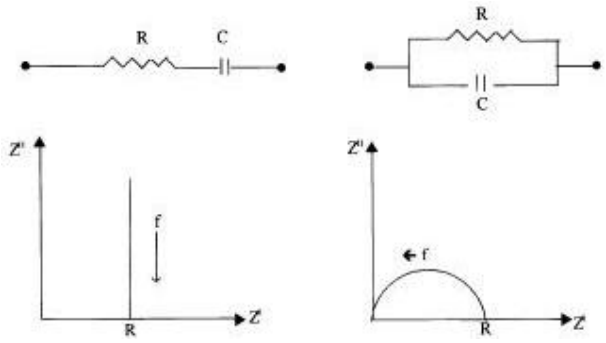


Figure3.4
Impedance plots for series and parallel combinations of *R* and *C*.

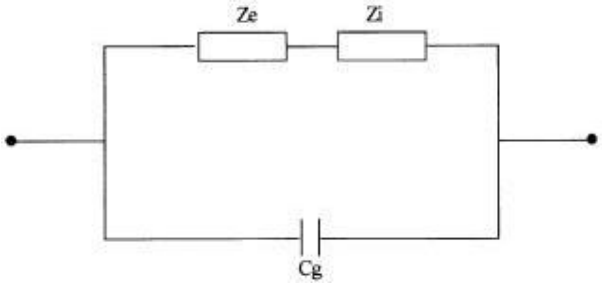


Figure3.5 Equivalent circuit of a symmetrical solid cell.

$Z_e$ is the bulk electrolyte impedance contribution, $Z_i$ the sum of both interface impedance contributions (on both sides of the electrolyte) and $C_g$ the geometrical cell capacity. The use of admittance plane plotting (Cole–Cole plot) for accurate conductivity determination of solid electrolytes was introduced by Bauerle (1969). An automatic system for frequency dependant impedance measurement based on computer controlled network which can measure up to 175°C was developed by Staudt (1981) and Schon (1989).

A microprocessor based Hewlett Packard 4192A low frequency impedance analyser was developed by Boukamp (1984), which overcomes the difficulty of measuring impedance in a specific range of frequency. The a.c. conductivity of solid electrolyte is analysed by Bruce and West (1983) in terms of equivalent circuit consisting of resistors and capacitors. They conducted two terminal a.c. measurements over the frequency range $10^3$–$10^7$ Hz using a combination of bridge and automated phase sensitive detection techniques. Balayaand Sunandana (1989) designed an electronic system based on quadrature oscillator, current–to–voltage converter and phase sensitive detector for measurement of a.c. conductivity and complex impedance over a range of frequencies up to 60 kHz.

It is evident from the review of literature that though bulk of the effort has gone into conductivity measurements by various techniques, very little work has been reported on the instrumentation aspects of the developed techniques. All the measuring techniques seem to be quite expensive and complex. To represent the given sample by pure electronic model calls for the use of complex impedance technique. The impedance spectrum is essential to obtain wealth of information about the sample. This spectrum can be obtained through several electronic techniques. From the above view points, it is clear that the complex impedance spectroscopic measurement of a.c. conductivity is a widely used method. Hence, a modest attempt is made here to develop an inexpensive, indigenous and simple electronic instrument for the measurement of real and imaginary parts of complex impedance of the given sample. The conductivity may be expressed by the known Arrhenius dependence is

$$\sigma = \sigma_0 \exp(-E/RT) \quad \text{(4)}$$

Here $\sigma$ is the conductivity and the effective activation energy E is a temperature independent constant whose value depends on the mechanism of conduction and T is the absolute temperature.

This form provides an accurate description of both ionic and electronic conductivities in ionic crystals. [43, 44]. After the sample resistance (grain and grain boundary resistance combined) has been determined from the Nyquist plot, the conductivity of the sample at a given temperature is calculated using the equation $\sigma = t/AR_{s,}$ where σ is the conductivity of the sample, $R_S$ is the sample resistance, A and t are the area and thickness respectively. The conductivity as a function of temperature follow the relationship ie. $\sigma = \frac{\sigma_0}{T}\exp(\frac{-\mathrm{E}a}{kT})$ where σ is total ionic conductivity, $\sigma_o$ is a pre-exponential factor, $E_a$ is the activation energy (in Joules), k is Boltzman's constant, and T is the temperature in Kelvins. Rearranging the following equation and taking the natural logarithm the conductivity equation can be expressed as:

$$\ln(\sigma T) = \ln\sigma_0 - Ea/kT$$

Plotting ln (σT) vs. 1/T an Arrhenius plot is produced. The data is then fit as a straight line and the activation energy can be determined from the slope of the graph (EA/k). [45].

## 3.4 Differential Thermal Analysis

It is a thermo analytic technique, similar to differential scanning calorimetry. In DTA, the material under study and an inert reference are made to undergo identical thermal cycles, while recording any temperature difference between sample and reference. This differential temperature is then plotted against time, or against temperature (DTA curve or thermogram). Changes in the sample, either exothermic or endothermic, can be detected relative to the inert reference. Thus, a DTA curve provides data on the transformations that have occurred, such as glass transitions, crystallization, melting and sublimation. The area under a DTA peak is the enthalpy change and is not affected by the heat capacity of the sample. A DTA consists of a sample holder comprising thermocouples, sample containers and a ceramic or metallic block; a furnace; a temperature programmer; and a recording system.

The key feature is the existence of two thermocouples connected to a voltmeter. One thermocouple is placed in an inert material such as $Al_2O_3$, while the other is placed in a sample of the material under study. As the temperature is increased, there will be a brief deflection of the voltmeter if the sample is undergoing a phase transition.

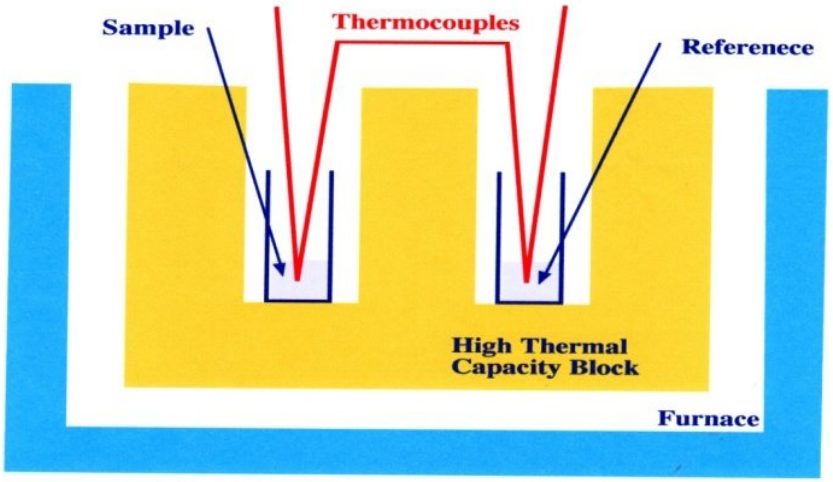


Figure 3.4 The Basic Differential Thermal Analysis Apparatus

This occurs because the input of heat will raise the temperature of the inert substance, but be incorporated as latent heat in the material changing phase [41].The established oven system is depicted in figure 3.4. The sample and the reference standard are placed in containers situated in two cavities contained in a high thermal capacity block. Thermocouples are situated in the sample and the reference materials and are connected in opposition so only a temperature difference between the two will be recorded. The reference standard must not suffer any change in state over the temperature range employed to examine the sample. Alumina and silicon carbide are satisfactory reference standards for solids whereas dinonyl phthalate and certain silicone oils have been used as standards for liquids. As the temperature is increased any change in phase by the sample will result in a negative or positive temperature signal from the thermocouples.

An alternative and probably a more popular system is shown in figure [3.5]. The sample and reference standard are placed in the furnace on flat, highly thermally conductive pans and the thermocouples are physically attached to the pans directly under the sample. This procedure avoids or reduces any thermal lag resulting from the time required for the heat to transfer to the sample and reference materials and then to the thermocouples. The thermocouples are connected in opposition in the same manner as the previous system.

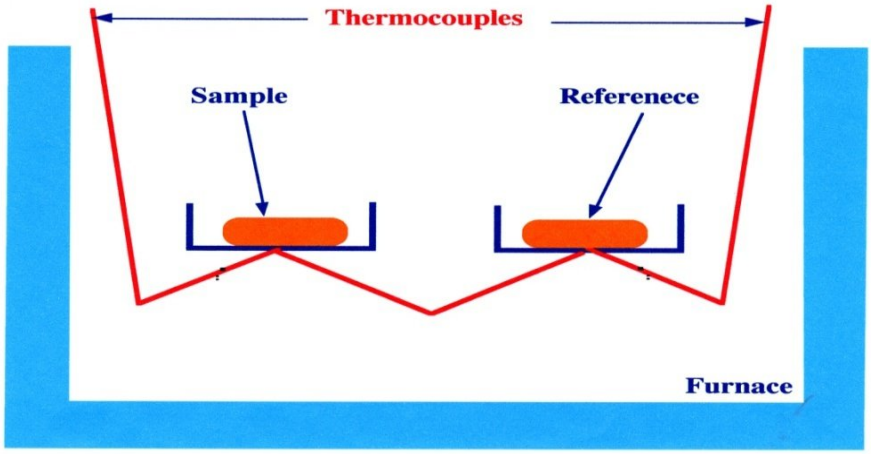


Figure 3.5. An Alternative Differential Thermal Analysis Apparatus

# CHAPTER–4 *EXPERIMENTAL PROCEDURE*

In this chapter, the procedure adopted to prepare samples from raw materials is described- in detail. The synthesized pallets were characterized by different technique. The details of this are described below:

## 4.1 Sample Preparation

The powders of each system were prepared by solid state reaction technique by taking required stochiometric amount of constituent oxides for the mentioned systems. Sample having the composition (100-x) $ZrO_2$(x) $Bi_2O_3$ for (x= 0, 5, 10, 15, 20, 25, 30, 35, 40, 45, 50) were prepared by taking initial ingredients $Bi_2O_3$ (99%, Loba chemical) and $ZrO_2$ (99.9%, Sigma Aldrich). Both chemicals were used without any purification. The required amounts of chemicals were mixed and grinded with hand in wet medium (acetone AR grade) using agate mortar pestle for two hours to reduce the particle size. The resulting mixture was dried in air. After mixing this powder was taken in silica crucible and calcination was done at various temperatures. After calcination these powders were again taken in agate mortar pestle and grinded with hand in wet medium (acetone AR grade) for two hours to reduce the particle size, as well as to homogenise the calcined powder. Further all the samples with composition more than 15% $Bi_2O_3$ were sintered at 800°C. Since the samples with higher concentration of $Bi_2O_3$ (more than 25% ) results in partial melting, so we have limited our study on three samples with compositions (15 mol% Bi $_2O_3$ with 85 mol% $ZrO_2$, 20 mol% $Bi_2O_3$ with 80mol% $ZrO_2$ and 25 mol% $Bi_2O_3$ with 75mol% $ZrO_2$) only. The details of sample composition are given in table 4.1.

**Table 4.1** The detail of samples and their processing conditions (calcinations and sintering).

| Mol% | Calcination (°C ) | Sintering (°C) | Appearance after calcination | Appearance after sintering | Calcine temp. (hour) | Sinter temp. (hour) | Green Density ($g/cm^3$) |
|---|---|---|---|---|---|---|---|
| 5 mol% $Bi_2O_3$ with 95 mol% $ZrO_2$ | 900 | 1100,1050,1000 Three samples at different temp. | Light yellow | Dark yellow | 12 | 24 | 4.348, 4.406, 4.353 |
| 10 mol% $Bi_2O_3$ with 90 mol% $ZrO_2$ | 900 | 2 samples at 1050 and 2 samples at 1000 temp. | Light yellow | Dark yellow | 12 | 24 | 4.615, 4.618, 4.531, 4.679 |
| 15 mol% $Bi_2O_3$ with 85 mol% $ZrO_2$ | 900 | 2 samples at 800 | Some more Yellow | Dark yellow very uniform | 12 | 24 | 4.868, 4.911 |
| 20 mol% $Bi_2O_3$ with 80 mol% $ZrO_2$ | 800 | 2 samples at 800 | Some more Yellow | Much dark yellow | 12 | 24 | 5.055, 5.195 |
| 25 mol% $Bi_2O_3$ with 75 mol% $ZrO_2$ | 800 | 2 samples at 800 | Yellow colour get | Much than above dark yellow | 12 | 24 | 5.281, 5.261 |
| 30 mol% $Bi_2O_3$ with 70 mol% $ZrO_2$ | 800 | 2 samples at 800 | Some more yellow get but partially melt | Very dark yellow and radish colour | 12 | 24 | 5.474, 5.464 |
| 35 mol% $Bi_2O_3$ with 65 mol% $ZrO_2$ | 800 | 2 samples at 800 | Some more than above yellow but partially melt | Very dark yellow and radish colour | 12 | 24 | 5.595, 5.584 |
| 40 mol% $Bi_2O_3$ with 60 mol% $ZrO_2$ | 800 | 2 samples at 800 | Dark yellow get but partially melt | Very dark yellow and radish colour | 12 | 24 | 5.724, 5.713 |
| 45 mol% $Bi_2O_3$ with 55 mol% $ZrO_2$ | 800 | 2 samples at 800 | light oranges colour get but partially melt | Very dark yellow and radish colour | 12 | 24 | 5.980, 5.769 |
| 50 mol% $Bi_2O_3$ with 50 mol% $ZrO_2$ | 800 | 2 samples at 800 | Dark Yellow but partially Melt | Very dark yellow and radish colour | 12 | 24 | 6.007, 5.932 |

### 4.2 Pellets Preparation

The calcined powders were crushed again and mixed with 5 drops of polyvinyl alcohol (PVA) of 10 weight% solution in water. The mixed green powder was compacted at 10 tons pressure in a die. The dimensions of pellet were of 20mm diameter with thickness 2mm to 3mm respectively.

### 4.3 Sintering

The pellets of compositions (15 mol% $Bi_2O_3$ with 85mol% $ZrO_2$, 20 mol% $Bi_2O_3$ with 80mol% $ZrO_2$ and 25 mol% $Bi_2O_3$ with 75mol% $ZrO_2$) obtained after compaction were sintered in air at 800°C for 24 hours in calibrated tubular furnace. For sintering of pallets a bed of same composition was made on alumina plate to avoid contamination (if any. Another samples 40 mol% $Bi_2O_3$ with 60 mol% $ZrO_2$ and 50 mol% $Bi_2O_3$ with 50 mol% $ZrO_2$ were also sintered at 750°C to optimize the processing condition for achieving better properties. The flow sheet of the experimental procedure adopted is given below in figure 4.1.

The characterization techniques used for the sintered pallets are explained below:

### 4.4 Phase identification (XRD)

XRD technique was used to determine the state of chemical combination of the constituent components involved for the preparation of pallets and phase present in the system. The powders of samples I, II and III were characterized by X-ray diffraction analysis and the peaks were marked on the basis of ICDD data base. XRD measurements were done using Panalytical X'Pert Pro system with monochromatic Cu Kα radiation having wavelength (λ= 1.54 Å). The data were collected for all samples at room temperature in the range of $20° \leq 2\theta \leq 80°$ at the scan speed of 5°/ min.

### 4.5 Thermal study (TG/DTA)

DTA curve provides information as well as data of the transformations that have occurred, such as glass transitions, crystallization, melting and sublimation. Moreover, changes are observed in

the samples relative to the inert reference sample and these changes are observed in terms of either exothermic or endothermic peaks. The weight changes of $ZrO_2$ and $Bi_2O_3$ powders with change in temperature during heating were monitored by the thermo gravimetric analysis (TG/DTA). The powders were heated from 50°C to 800°C at rate of 10°C/min in nitrogen ($N_2$) atmosphere as well as in argon atmosphere. The thermal studies were carried out for all the three samples as mentioned earlier.

### 4.6 Electrical conductivity

Electrical conductivity was measured from the complex impedance spectra of the samples using Model 4274 multi-frequency Hewlett-Packard LCR meter. These impedance spectra were obtained by plotting the real part Z′ against imaginary part Z″ at temperatures from 120$^{o}$C - 800$^{o}$C and in the frequency range from 100 Hz-100 kHz as shown in figures 5.6 and 5.7. For ionic conductivity measurement, both side surfaces of the specimens were coated with gold. The specimen was heated up to 800°C at a rate of 10°C/min and held for 1-2 minute at each temperature for thermal equilibration prior to measuring conditions at that temperature. The ionic conductivity of all the sintered samples measured as a function of temperature.

### 4.7 Microstructural analysis (SEM)

The microstructural study was carried out on flat surfaces of all the samples by scanning electron microscope (SEM). For it all the samples were coated with gold to observe the micro structure.

**Table 4.1** Sample label with different compositions

| S. No. | Sample Label | $ZrO_2$ composition | $Bi_2O_3$ composition |
|---|---|---|---|
| **1.** | Sample I | 85mol% | 15 mol% |
| **2.** | Sample II | 80mol% | 20 mol% |
| **3.** | Sample III | 75mol% | 25 mol% |

**Figure 4.1** Flow chart of the experimental procedure

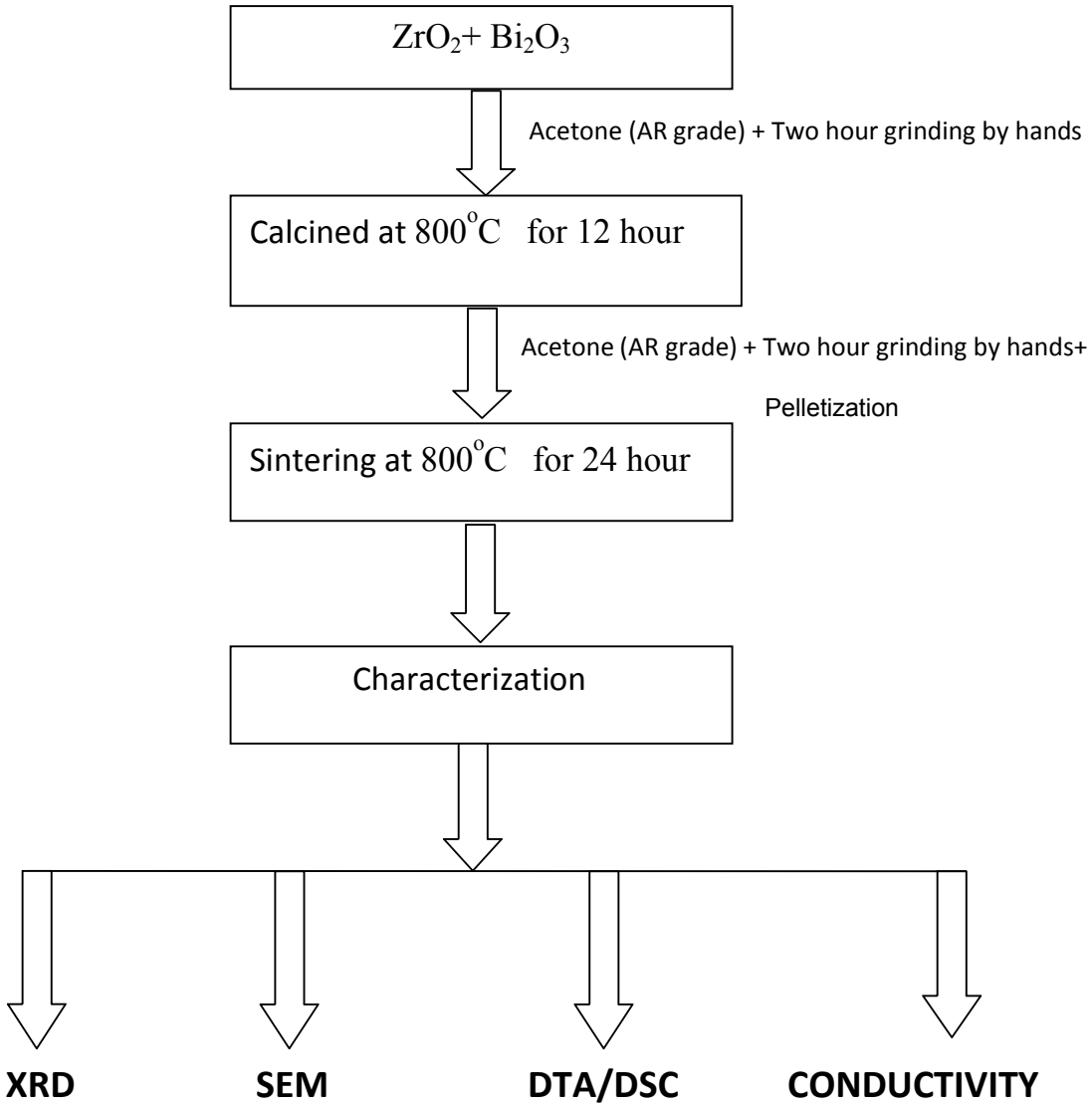

## 5.1 X-Ray Analysis

The X-ray diffraction patterns of composition (100-x) $ZrO_2$ (x) $Bi_2O_3$ are given below in the figure 5.1. The XRD pattern indicates that all the compositions exhibit Zirconium Bismuth Oxide. Apart from this, $ZrO_2$ and $Bi_2O_3$ individual phases were also present. In other words, the XRD pattern exhibits the mixed phase in all the samples. The main phase present was $Bi_{1.85}Zr_{0.15}O_{3.075}$ with reference code. 01-070-7693. the remaining unreacted phases were of $ZrO_2$ and $Bi_2O_3$ . They were indexed with the reference codes of 01-078-0047 and 01-074-1375 respectively. The phase $Bi_{1.85}Zr_{0.15}O_{3.075}$ was found to exhibit tetragonal structure. Whereas, $ZrO_2$ and $Bi_2O_3$ phases found to exhibit monoclinic and cubic structures respectively. The volume fraction of $Bi_{1.85}Zr_{0.15}O_{3.075}$ along with $ZrO_2$ and $Bi_2O_3$ phases was calculated for all three samples I, II and III respectively as indicated in table 5.1. It was observed that volume fraction of $Bi_{1.85}Zr_{0.15}O_{3.075}$ phase increases slightly with increase in $Bi_2O_3$ content and was found to be maximum in sample III as indicated in table 5.1. On the other hand, $ZrO_2$ phase slightly decreases in samples II and III with increase in $Bi_2O_3$ content as indicated in figure 5.1. Similar results have been also reported by Abraham et.al. [23]. Moreover, the peaks of $Bi_{1.85}Zr_{0.15}O_{3.075}$ phase shifts slightly towards lower angle with minute peak broadening with increasing doping contents of $Bi_2O_3$ in $ZrO_2$. It means that the disordering increases in the samples as shown in the XRD pattern of these compositions. It is also confirmed by the lattice parameters calculations of the particular phase. The XRD pattern also indicates that no solid solution has formed in the present samples. Moreover, sample III exhibiting maximum disorderness also shows the highest value of electrical conductivity with maximum density as indicated in table 5.2. In other words, as the percentage of $Bi_2O_3$ increases in the matrix of $ZrO_2$, then disordering increases in the system leading to one order higher conductivity in sample III as compare to samples I and II.

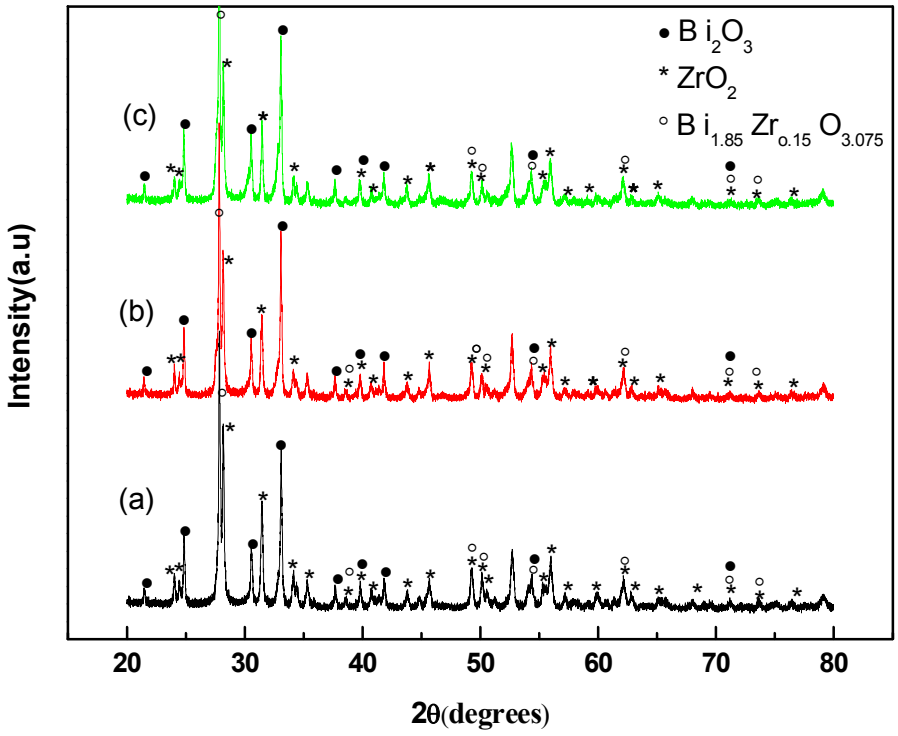


**Figure 5.1** X-ray diffraction patterns of (100-x) $ZrO_2$(x) $Bi_2O_3$ for (a) 15 mol% $Bi_2O_3$ with 85 mol% $ZrO_2$, (b) 20 mol% $Bi_2O_3$ with 80mol% $ZrO_2$ and (c) 25 mol% $Bi_2O_3$ with 75mol% $ZrO_2$

The XRD pattern of these samples also indicates that no solid single phase is formed in the present compositions. It was observed that the very small Zr substitutes for Bi in $Bi_{1.85}Zr_{0.15}O_{3.075}$ phase [46].

**Table 5.1** Lattice parameters of $Bi_{1.85}Zr_{0.15}O_{3.075}$ and volume fraction calculated for different phases present in samples I, II and III.

| S. No. | Samples | a( Å) | c (Å) | Volume Fraction | | |
|---|---|---|---|---|---|---|
| | | | | $Bi_{1.85}Zr_{0.15}O_{3.075}$ | $Bi_2O_3$ | $ZrO_2$ |
| 1. | I | 7.82 | 5.54 | 43.3 | 20.8 | 35.86 |
| 3. | II | 7.84 | 5.56 | 44.3 | 20.74 | 34.86 |
| 4. | III | 7.852 | 5.57 | 45.16 | 20.91 | 33.89 |

## 5.2 Thermal Analysis

The TG/DTA studies were carried out in nitrogen atmosphere as well as in argon atmosphere from $50^0$C to $800^0$C at a heating rate $10^0$C/min as shown in figures 5.2, 5.3, 5.4 and 5.5 respectively. All the graphs indicate weight loss below 200°C temperature. It might have incurred because of release of adsorbed water associated with crystalline structure [48]. Second peak in all the samples between 350°C and 400°C can be designated due to phase transition. This can be correlated with similar phase transition observed in electrical conductivity measurement. Moreover, it was observed that in nitrogen atmosphere, the changes in TGA curve is more prominent in sample III. On the other hand, the changes in the same sample become minute when TGA was performed in Argon atmosphere. It again indicates clearly that sample III exhibits higher oxygen vacancies as well as higher density with lesser porosity. The higher value of conductivity obtained in sample III verify the above hypothesis. In addition to this, sample III exhibits no significant weight change in nitrogen atmosphere signifying greater stability of this sample.

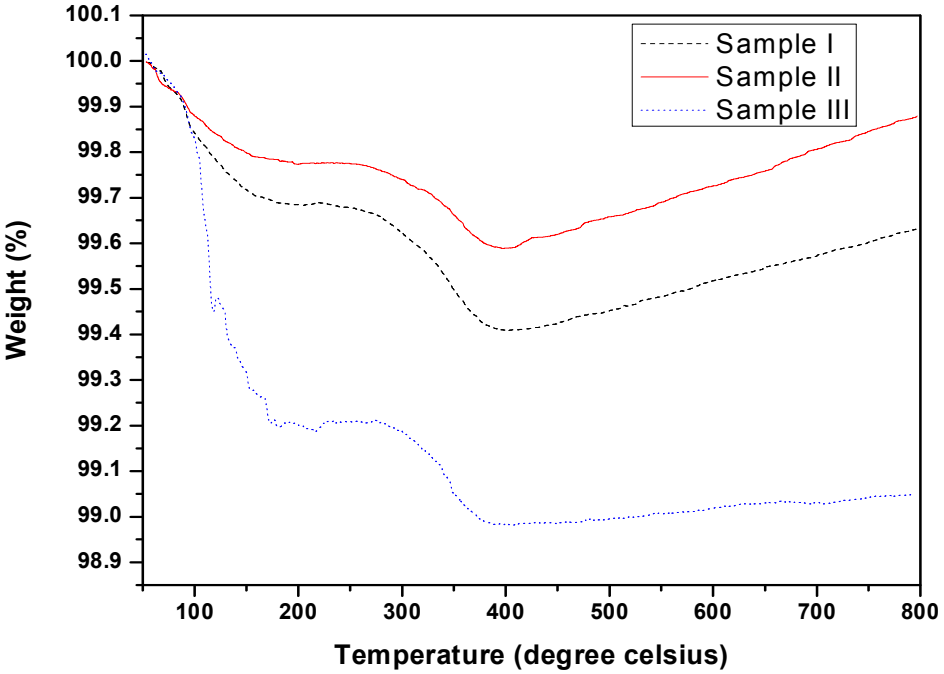


**Figure 5.2:** TGA of sample I, sample II and sample III in nitrogen atmosphere.

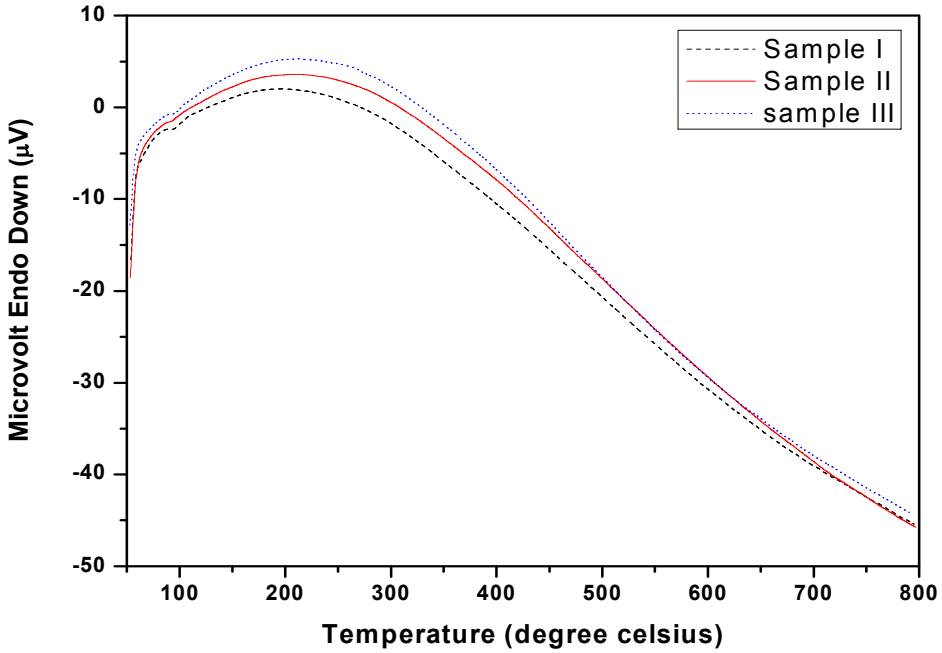


**Figure 5.3:** DTA of sample I, sample II and sample III in nitrogen atmosphere.

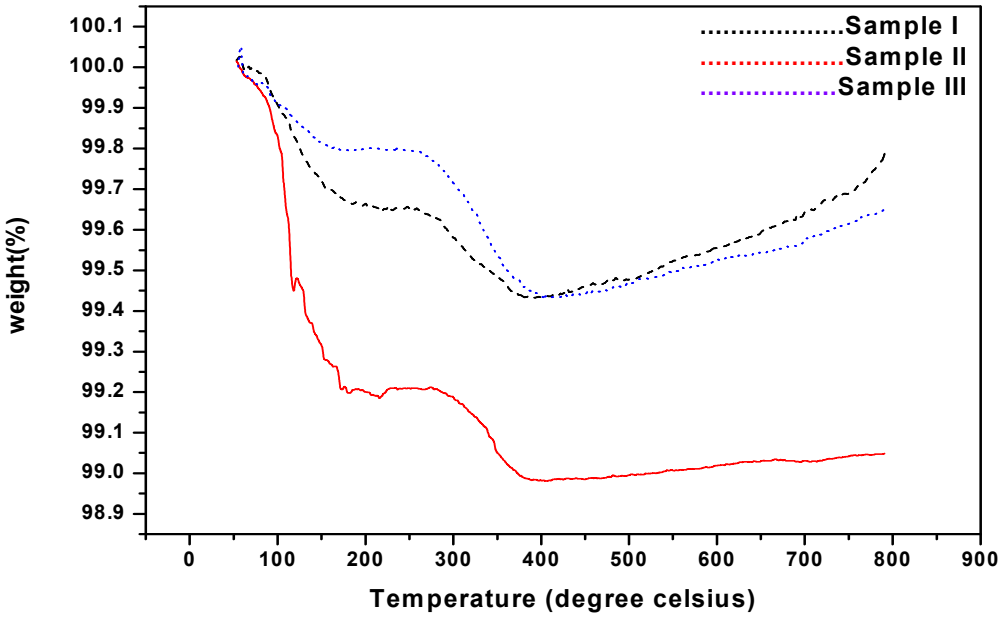


**Figure 5.4:** TGA of sample I, sample II and sample III in argon atmosphere.

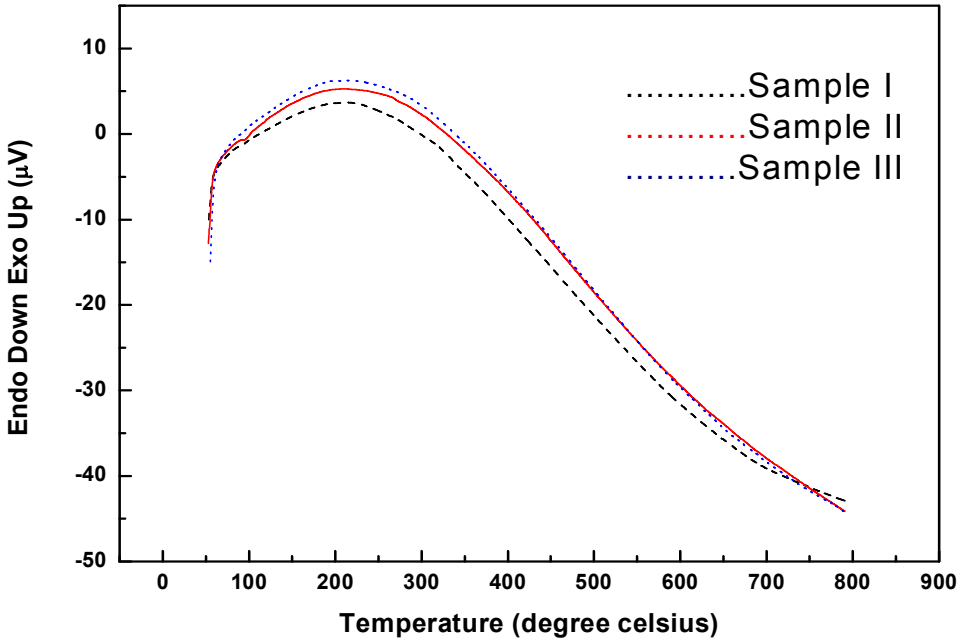


**Figure 5.5:** DTA of sample I, sample II and sample III in argon atmosphere.

## 5.3 Electrical conductivity

The total resistance of the samples at various temperatures was determined from the point of intersection of the spectrum with the real axis and converted into conductivity using the following relation:

$$\sigma = \frac{l}{RA} \qquad \text{(i)}$$

Where l is the thickness of the pellet and A is cross-sectional area of the pellet. With increasing temperature the resistance of the sample drops and conductivity increases which is manifestation of high temperature ionic conductors. The selected impedance spectra of samples I and II in the temperature interval from 360°C to 680°C and in the frequency range from 100 Hz to 100 kHz has been shown in figure 5.6 and 5.7 respectively. It was observed that the resistivity of the sample-to-electrode contact had an influence on the sample conductivity at higher temperature of 680°C. Similar behaviour was reported by Zdujic et.al. [48]. The Arrhenius plot of all the three samples is shown in figures 5.8, 5.9 and 5.10 respectively. The fluctuations from 350°C to 400°C were observed in all three samples I, II and III which may occur due to phase transition. These fluctuations were also observed in TGA results of all three samples. On the other hand, these fluctuations get subsidized in sample III; linear region extends up to nearly 350°C in sample II and 440°C in sample III. In other words, the arrhenius plot of sample III shows two linear regions between 280°C to 420°C and 560°C to 700°C. Similar behaviour is exhibited by $Bi_{1.89}Zr_{0.11}O_{3.055}$ system as reported by Abraham et.al. [23]. Moreover, there is change of one order of conductivity observed in sample III due to higher disordering present in the sample. The conductivity values for all the samples are calculated and summarized in table 5.2. The conductivity of samples I, II and III come out to be of almost similar order as observed in some reported data [23]. However, the conductivity decreases slightly in sample II. It might be associated with slight ordering induced by the $Bi^{3+}$ substitution up to x=0.20. The TGA results also support increasing ordering in this sample. The conductivity difference between samples II

and III can be explained on the basis of the order-disorder transition and transition becomes prominent with doping of higher amount of $Bi_2O_3$ content due to intrinsic electronic disorder.

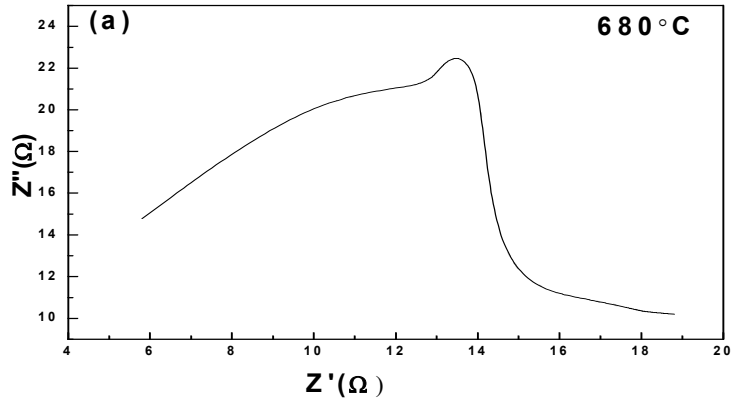


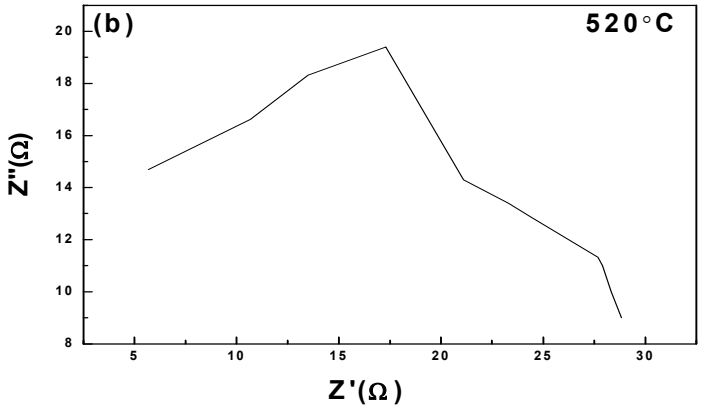

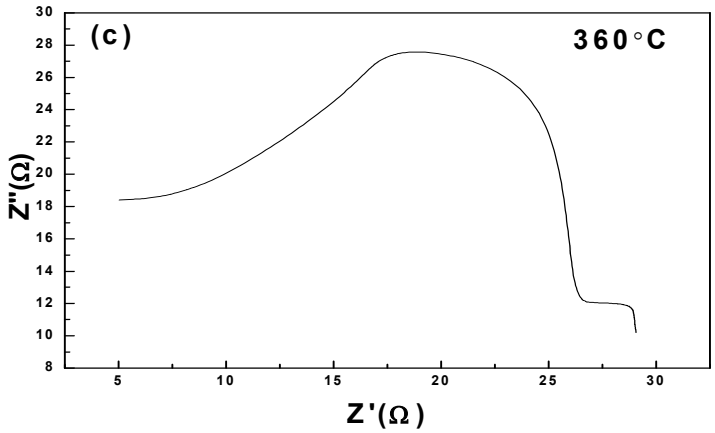


**Figure 5.6** Impedance spectra of sample I during cooling cycle at various temperatures.

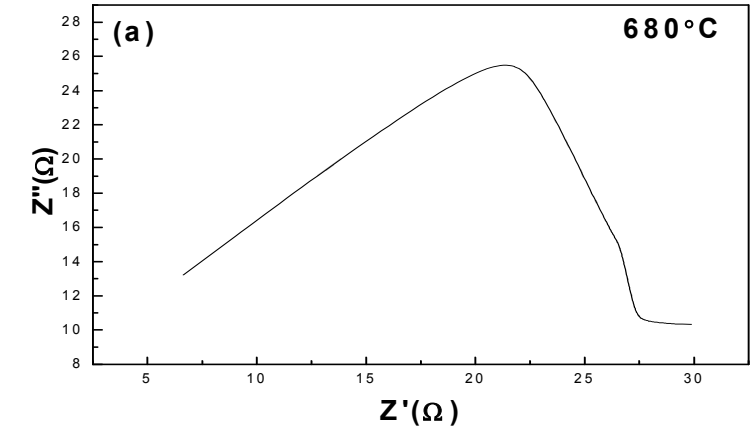


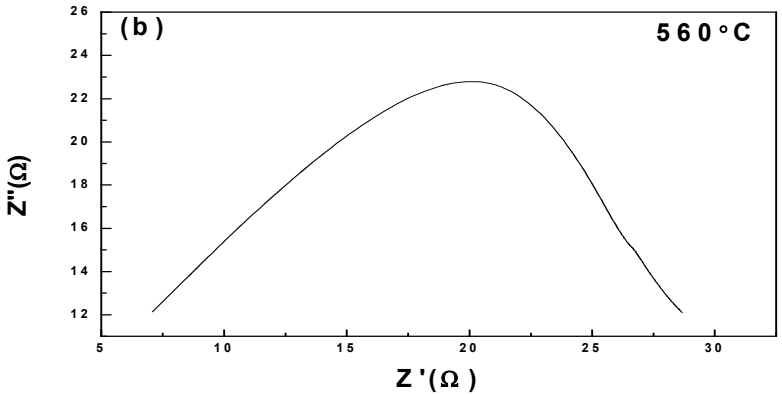

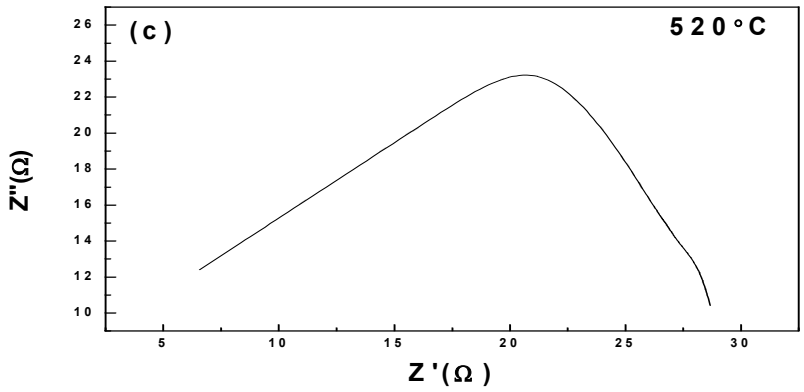


**Figure 5.7** Impedance spectra of sample II during cooling cycle at various temperatures.

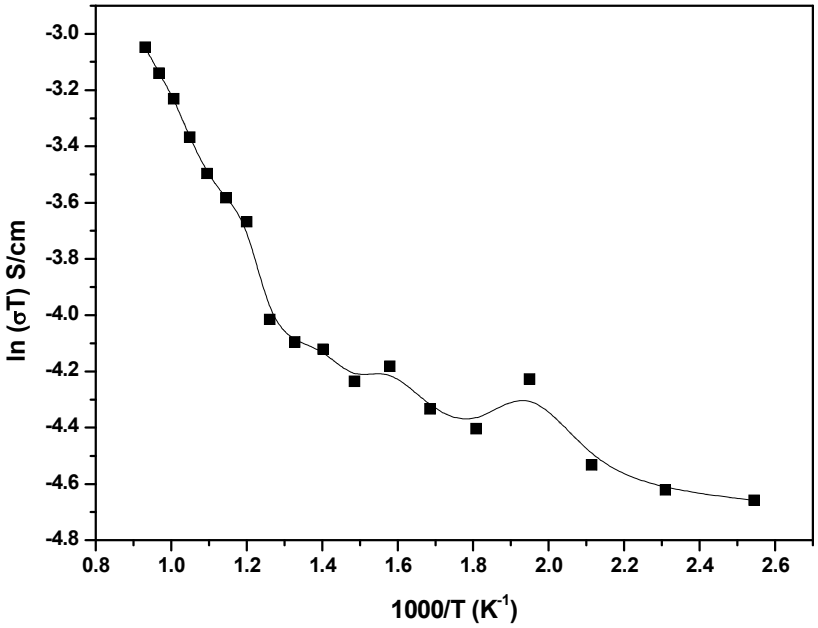


**Figure 5.8** Arrhenius plot of conductivity for sample I during cooling cycle

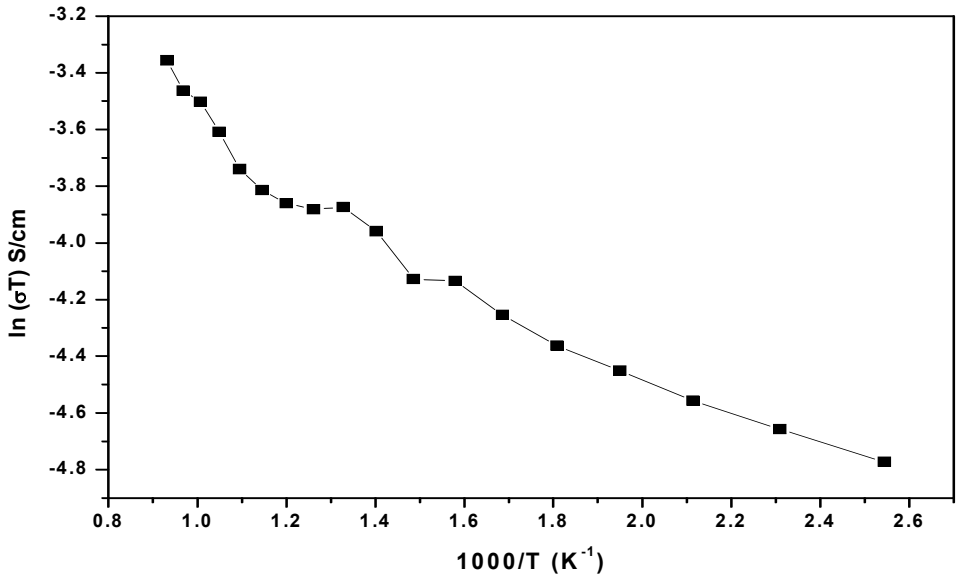


**Figure 5.9** Arrhenius plot of conductivity for sample II during cooling cycle

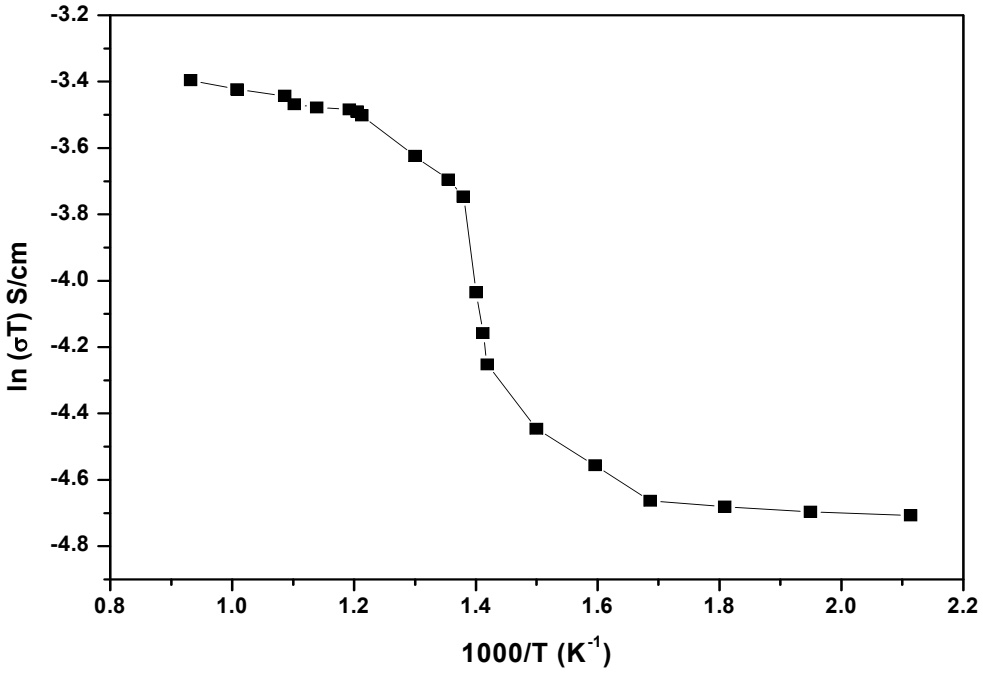


**Figure 5.10** Arrhenius plot of conductivity for sample III during cooling cycle

**Table 5.2** Comparison of the conductivity (S $cm^{-1}$) of the samples at 400 $^0$C and 800 $^0$C along with their density and relative density.

| S .No. | Sample Level | σ (S $cm^{-1}$) at 400$^0$C | σ (S $cm^{-1}$) at 800$^0$C | Density ($g/cm^3$) | Relative Density (%) |
|---|---|---|---|---|---|
| 1. | Sample I | 2.15 X$10^{-5}$ | 4.43X$10^{-5}$ | 5.53 | 89.7 |
| 2. | Sample II | 2.39 X$10^{-5}$ | 3.24 X$10^{-5}$ | 5.19 | 82.1 |
| 3. | Sample III | 3.03 X$10^{-5}$ | 4.21 X$10^{-4}$ | 6.73 | 98 |

### 5.4 Microstructural analysis (SEM)

The microstructural study was carried out on flat surfaces of all the samples and all the surfaces were coated with gold to see the micro structure. The micrographs are presented below:

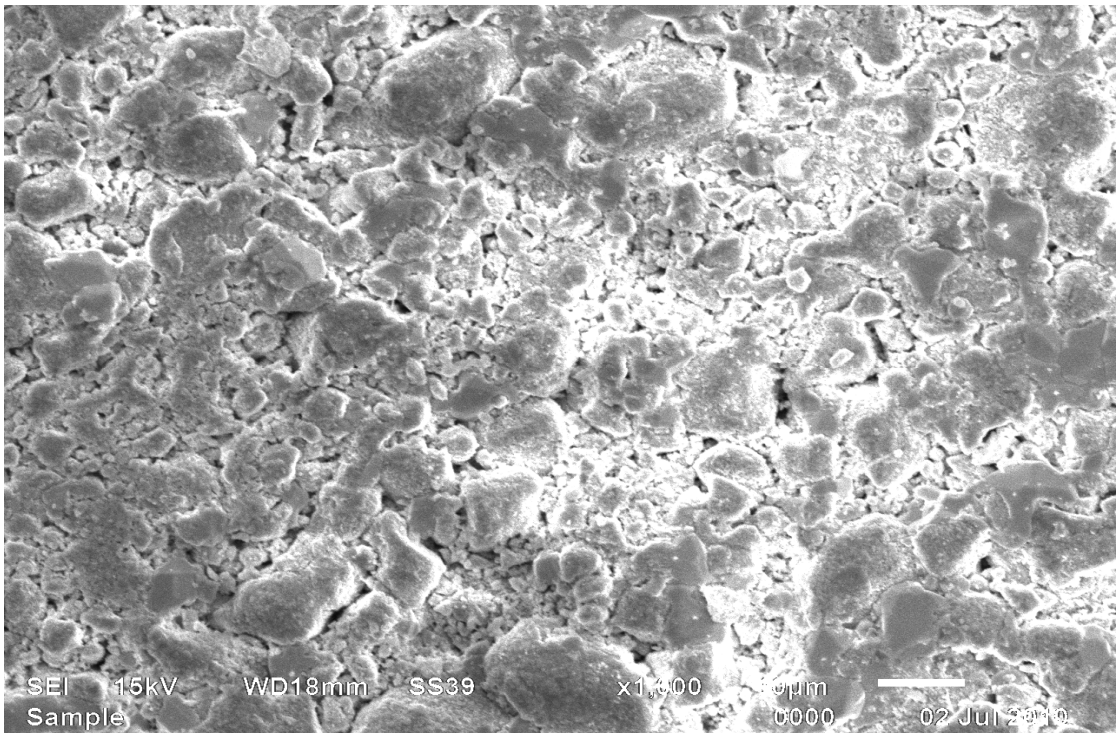


Fig.5.4.1 SEM image of Sample I (15 mol% $Bi_2O_3$ with 85mol% $ZrO_2$) at 1000× magnification.

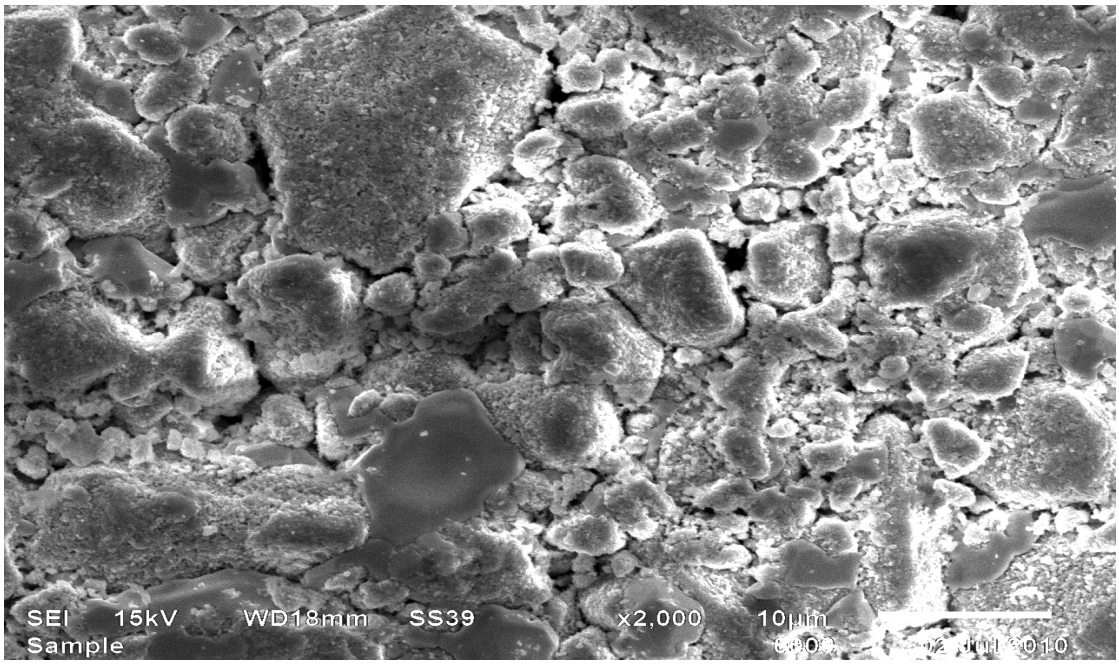


Fig.5.4.2 SEM image of Sample I (15 mol% $Bi_2O_3$ with 85mol% $ZrO_2$) at 2000× magnification.

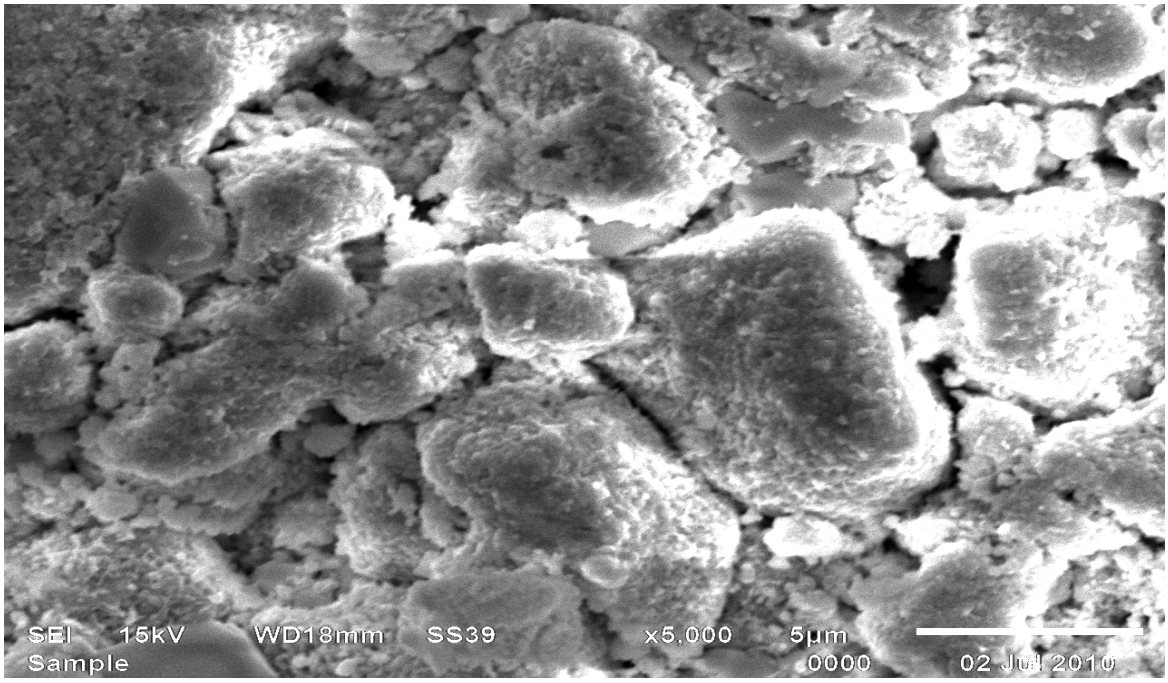


Fig.5.4.3 SEM image of Sample I (15 mol% $Bi_2O_3$ with 85mol% $ZrO_2$) at 5000× magnification.

.

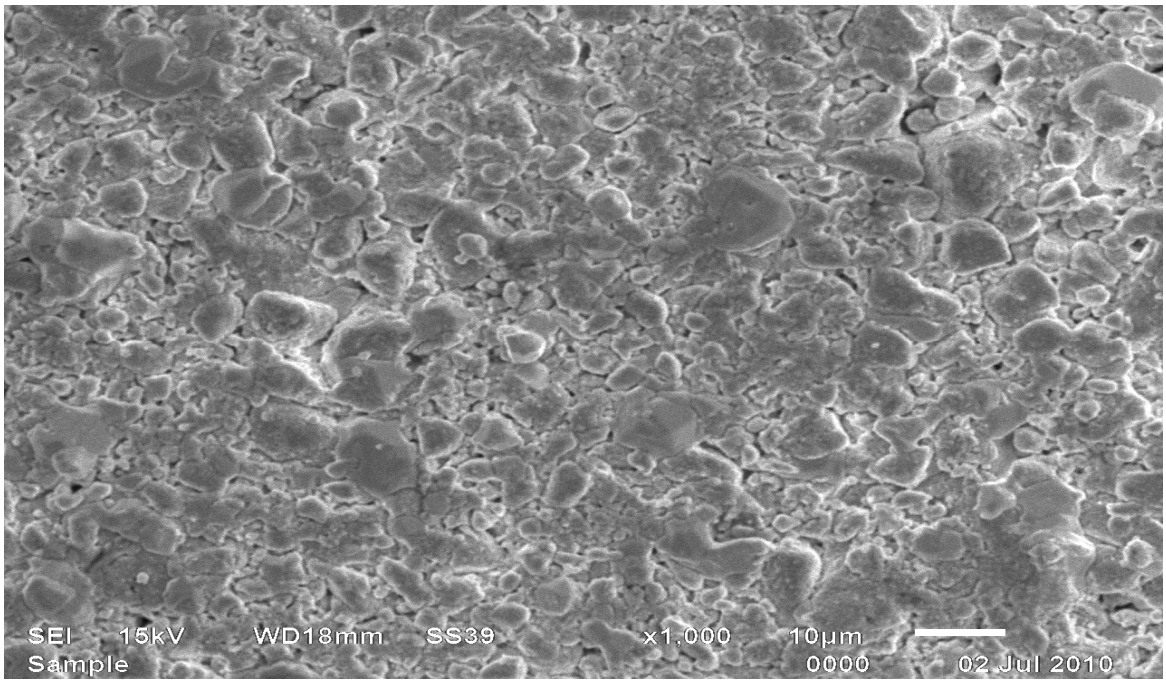


Fig.5.4.4 SEM image of Sample II (20 mol% $Bi_2O_3$ with 80mol% $ZrO_2$) at 1000× magnification.

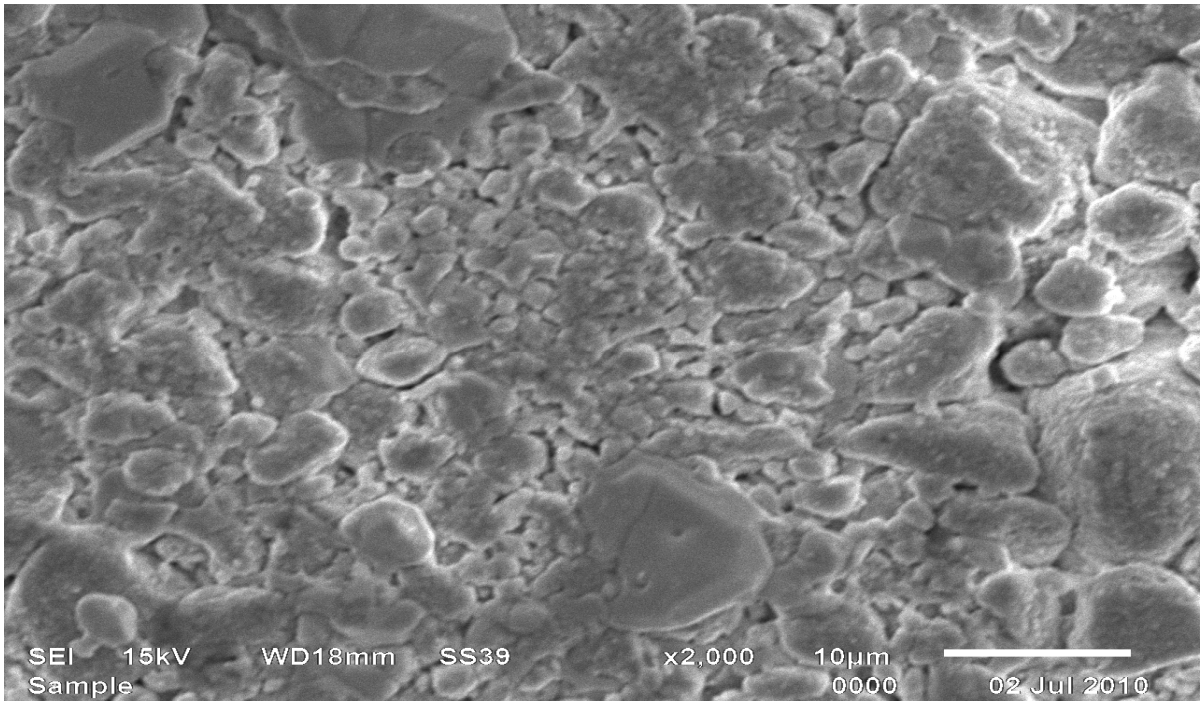


Fig.5.4.5 SEM image of Sample II (20 mol% $Bi_2O_3$ with 80mol% $ZrO_2$) at 2000× magnification.

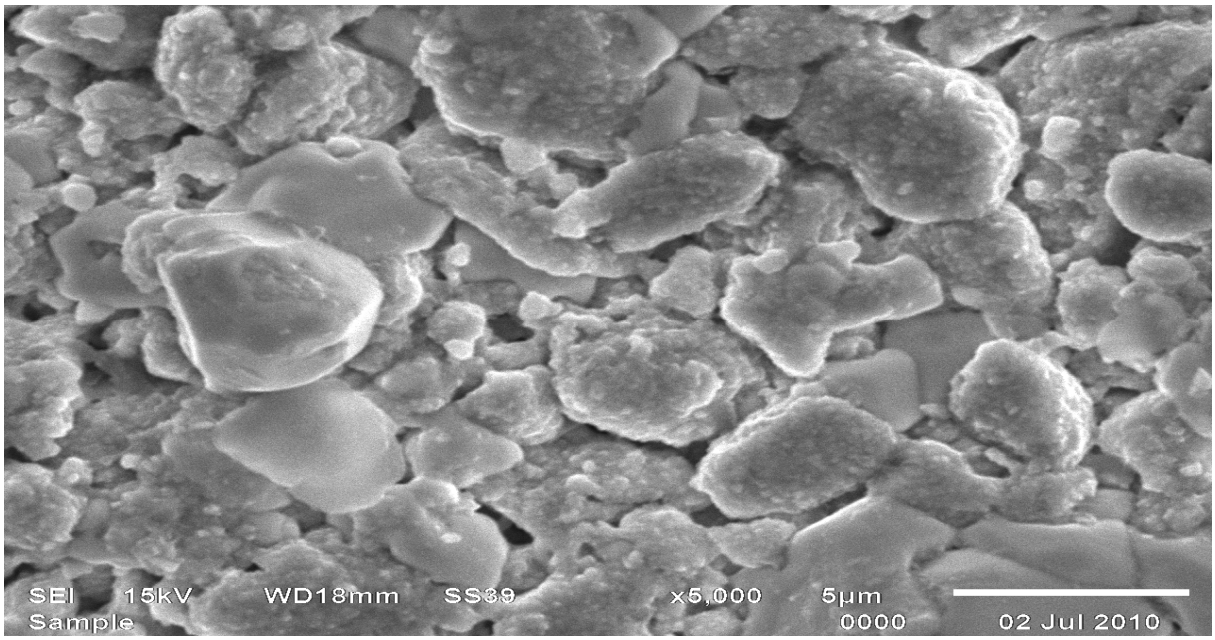


Fig.5.4.6 SEM image of Sample II (20 mol% $Bi_2O_3$ with 80mol% $ZrO_2$) at 5000× magnification

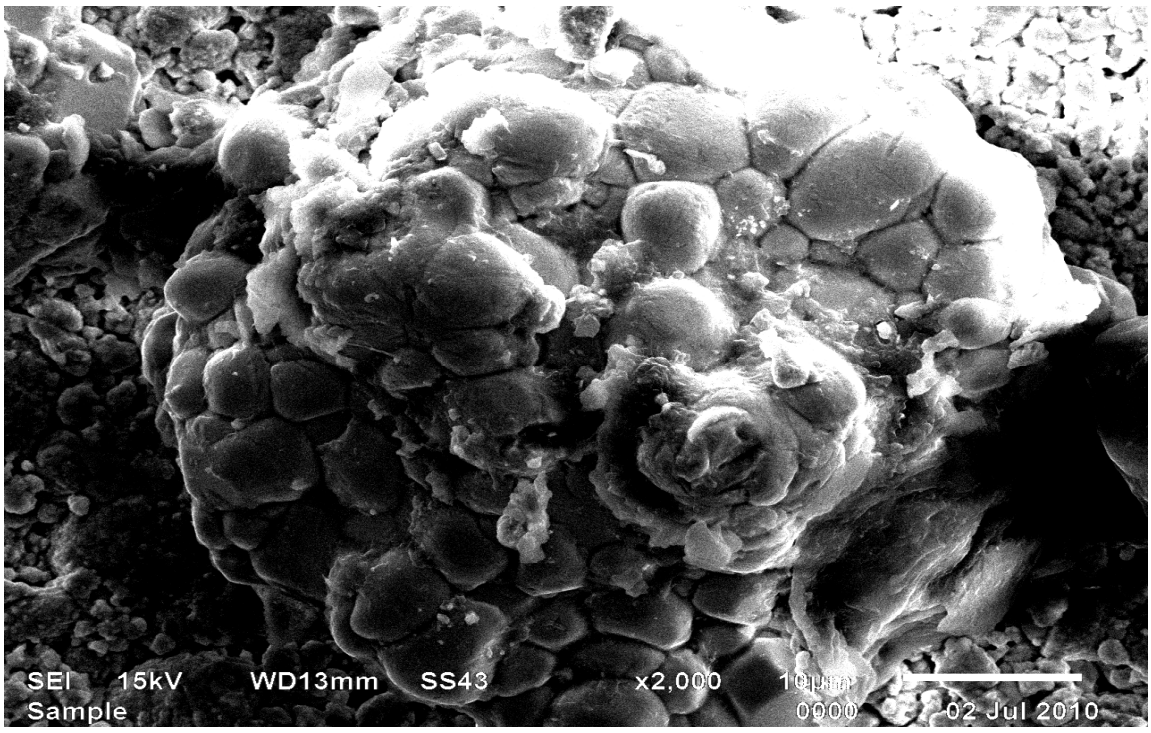


Fig.5.4.7 SEM image of Sample III (25 mol% $Bi_2O_3$ with 75mol% $ZrO_2$) at 2000× magnification

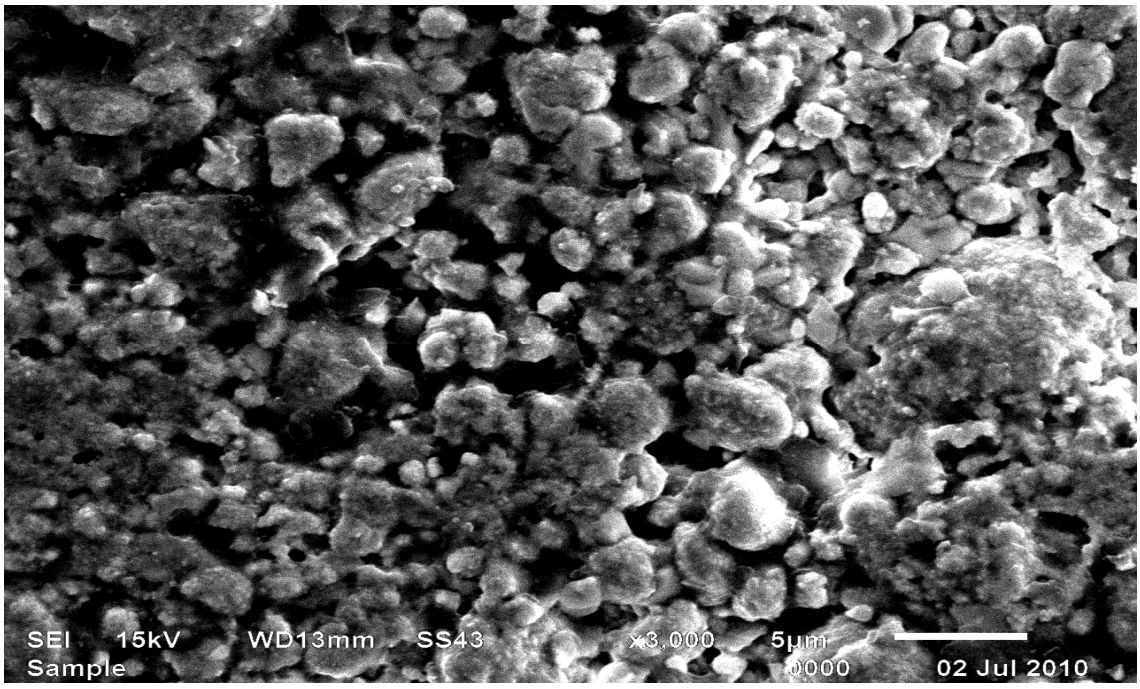


Fig.5.4.8 SEM image of Sample III (25 mol% $Bi_2O_3$ with 75mol% $ZrO_2$) at 3000× magnification

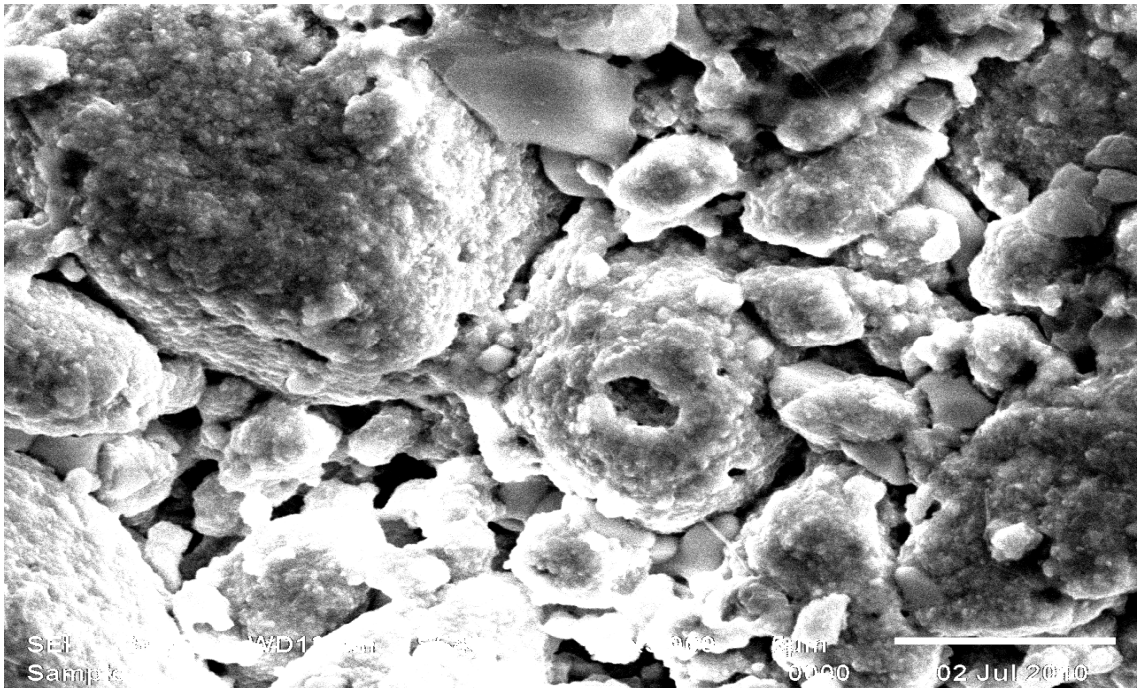


Fig.5.4.9 SEM image of Sample III (25 mol% $Bi_2O_3$ with 75mol% $ZrO_2$) at 5000× magnification

The microstructure of $ZrO_2$-$Bi_2O_3$ varies with the amount of $Bi_2O_3$, sintering temperature, and sintering time significantly. Large pores of several micrometers in diameter were clearly visible in all the micrographs. Microstructures were analyzed with respect to sintering temperature, time, and the amount of $Bi_2O_3$ in $ZrO_2$. Figure 5.4.1, 5.4.2 and 5.4.3 shows the flat surfaces of sample I sintered at 800°C for 24 hours. Figure 5.4.1 was at lower magnification i.e. 1000X and figure 5.4.2 was at higher magnification of 2000X and figure 5.4.3 was at magnification of 5000X. After sintering, the relative density of the Sample I came out to be nearly 89.7 % which means that significant densification and grain growth had occurred at 800°C. At magnification of 2000X in figure 5.4.2 we could clearly observe that there were two types of grains of different sizes. In the figure 5.4.3 the situation was same but magnification was high. Figure 5.4.4 was another SEM image of Sample II sintered at 800 °C for 24 hours. This figure was taken at magnification of 1000X. Figures 5.4.5 and 5.4.6 represents micrographs of same sample II at higher magnification of 2000X and 5000X. Figures 5.4.7, 5.4.8 and 5.4.9 showed the SEM-micrographs of sample III. They were having micrographs at magnification 2000X, 3000X, and 5000X respectively. They all were sintered at 800 °C for 24 hours. The grain size range of all SEM micrograph of different compositions at different magnifications is given below. Table 5.3 indicates that grain size of samples decreases with increase in $Bi_2O_3$ content. This decrease in grain size result in achieving highest density in sample III as clearly indicated in table 5.2. Moreover, in case of sample III, the grains were more closely packed with each other indicating that higher concentration of $Bi_2O_3$ leads to better sintering resulting in higher density. In addition to this, various grain shapes were clearly visible in all the micrographs. Whereas, it is not possible to distinguish $Bi_2O_3$ ad $ZrO_2$ phases present in the micrographs. However, the grain of unequal sizes appears to be distributed non-uniformly throughout the sample. Thus, it can be concluded that maximum density of sample III leads to the higher conductivity measurement.

**Table 5.3** Grain size ranges of the SEM micrograph at different magnification.

| Fig .No. | Compositions | Magnification | Grain Size Range (µm) |
|---|---|---|---|
| 5.4.1 | 15 mol% $Bi_2O_3$ with 85mol% $ZrO_2$ | 1000X | 1.998-17.316 |
| 5.4.2 | 15 mol% $Bi_2O_3$ with 85mol% $ZrO_2$ | 2000X | 1.665-18.081 |
| 5.4.3 | 15 mol% $Bi_2O_3$ with 85mol% $ZrO_2$ | 5000X | 0.920-7.921 |
| 5.4.4 | 20 mol% $Bi_2O_3$ with 80mol% $ZrO_2$ | 1000X | 0.5-9.75 |
| 5.4.5 | 20 mol% $Bi_2O_3$ with 80mol% $ZrO_2$ | 2000X | 1.665-12.321 |
| 5.4.6 | 20 mol% $Bi_2O_3$ with 80mol% $ZrO_2$ | 5000X | 0.5985-5.586 |
| 5.4.7 | 25 mol% $Bi_2O_3$ with 75mol% $ZrO_2$ | 3000X | 1.11-4.329 |
| 5.4.8 | 25 mol% $Bi_2O_3$ with 75mol% $ZrO_2$ | 2000X | 1.332-7.659 |
| 5.4.9 | 25 mol% $Bi_2O_3$ with 75mol% $ZrO_2$ | 5000X | 0.665-4.322 |

As reported by Verkerk et. al. [49] the formation of such large pores is due to the dissolution of $Bi_2O_3$ into the surrounding YSZ agglomerates leaving behind large pores. This is supported by the fact that the particle size of the as-received $Bi_2O_3$ powder is approximately the same as the average size of the large pores [46]. To examine the origin of these large pores we can prepare by pre-sintering as-received $Bi_2O_3$ and sieving pre-sintered $Bi_2O_3$ powder. One of the important features observed while comparing the micrographs of sample I, sample II, and sample III, is that the structure of sample III is different than other two samples. The sample undergoes sintering which causes the shrinkage and leads to formation of pores. These pores are filled by excess $Bi_2O_3$ during sintering as one can see the oozing out the structure in sample III at the surface. The flowery type structure seen clearly indicate this phenomenon. The presence of hole in these bigger particles indicates the volcanic type of eruptions (fig 5.4.9) which is only possible when the substance is thrown out from the matrix at the surface. The higher density also supports this action.

# Chapter-5 *CONCLUSIONS*

In the present work, $Bi_{1.85}Zr_{0.15}O_{3.075}$ electrolyte was synthesized by solid state reaction process. The X-ray diffraction confirmed the presence of unreacted $ZrO_2$ and $Bi_2O_3$ phases also. The XRD pattern of these samples also indicated that no single phase is formed in the samples studied in the present investigation. It was observed that volume fraction of $Bi_{1.85}Zr_{0.15}O_{3.075}$ phase increases slightly with increase in $Bi_2O_3$ content and was found to be maximum in sample III. Moreover, the peaks of $Bi_{1.85}Zr_{0.15}O_{3.075}$ phase slightly shifts towards lower angle with minute peak broadening with increasing doping contents of $Bi_2O_3$ in $ZrO_2$. It means that the disordering increases in the samples and becomes maximum in sample III as shown in the XRD pattern of these compositions. The XRD pattern also indicates that no solid solution is formed in the present samples. Moreover, it was observed that when TGA was done in nitrogen atmosphere, the changes in TGA curve is more prominent in sample III. On the other hand, the changes in the same sample become minute when TGA was performed in Argon atmosphere. It again clearly indicates that sample III exhibits higher oxygen vacancies as well as higher density with lesser porosity. Moreover, electrical conductivity of all three samples was done and change of one order of conductivity was observed in sample III due to higher disordering present in the sample as clearly indicated in XRD results. Finally we had observed the microstructure of all the three compositions. In this case we have seen some porous and some dense phase the dense phase is of $Bi_2O_3$ which was smooth in nature. The structural features of sample III is different than sample I and sample II. These arise because of liberation of $Bi_2O_3$ phase from inner core of the sample which causes different structural features.

## ***FUTURE SCOPE***

The study of zirconia based bismuth electrolyte, in the present thesis, was undertaken to establish potential applications in solid oxide fuel cell. The performance of solid oxide fuel cell depends primarily on ionic conductivity of electrolytes. Though yttria stabilized zirconia has been used as a base electrolyte in solid oxide fuel cell. However below $1000^{o}C$, its ionic conductivity decreases drastically. Therefore, new electrolytes which have good ionic conductivity in the temperature range of (500 to $800^{o}C$) are required to make cost effective SOFC. Thus, it can be interpreted from the above results that, if we increase the concentration of the dopant more than 25 mol%, then single phase $Bi_{1.85}Zr_{0.15}O_{3.075}$ compound may form and also conductivity may increases. Because such tetragonal phase are known to exhibit higher value of conductivity.

## *REFERENCES*


[1] C. Greaves. " The basic conversion of chemical energy into electricity", IOP Science, **5,** (1970).

[2] Timo Kivisaari, S.Thyberg Naumann, O.Lindstrom, and P.Bjornbom, AZ, **94**, (1992), 329-331.

[3] A.D Hawkes, L Exarchakos, D Hart, MA Leach, Ir. D. Haeseldonckx, Ir. L. Cosijns, Prof.Dr.Ir.W.D'haeseleer,"an introduction of fuel cells", Feb (2008).

[4] Eileen J. De Guire, review article, Solid Oxide Fuel Cells", April (2003).

[5] Robert J. Kee, Huayang Zhu and David G. Goodwin, **30,** January (2005), 2379-2404.

[6] B.H.C Steele, P.H. Middleton and R.A. Rudkin "Material science aspects of SOFC technology with special reference to anode development", **40-41,** august (1990), 388-393.

[7] X.J. Chen, K.A. Khor, S.H. Chan and L.G. Yu, J. Mater. Science and Engineering A, **335**, (2002), 246-252.

[8] A. Watanabe, "Phase equilibria in the system $Bi_2O_3$-$Y_2O_3$: no possibility of δ –$Bi_2O_3$ stabilization," Solid State Ionics", **86-88**, (1996), 1427-1430.

[9] J.W. Medernach and R.L. Snyder, "Powder diffraction patterns and structures of the bismuth oxides", J. Am. Ceram. Soc., **61,** (1978), 494-497.

[10] H.A. Harwig, "On the structure of bismuthsesquioxide: α, β, γ, and δ-phase", Z. Anorg. Allg. Chem., **444**, (1978), 151-166.

[11] M.W. Finnis and A.T. Paxton, "Crystal structures of zirconia from first principles and self-constant tight binding," Phys. Rev. Lett., **81**, (1998), 5142-5152.

[12] S. Ho, "On the structural chemistry of zirconium oxide," Materials Science and Engineering, **54**, (1982), 23-29.

[13] T. Takamori and M.W. Shafer, "Phase transformation kinetics in the system bismuth oxide-zirconia," J. Am. Ceram. Soc., **73**, (1990), 1453-1455.

[14] V. F. Hund, "Fluoritmischphsender dioxide von uran, thorium, cerund zirconium mit wismutoxid," Z. Anorg. Allg. Chem., **333**, (1964), 248-255.

[15] L. Sorokina and A.W. Sleight, "New phases in the $ZrO_2$-$Bi_2O_3$ and $HfO_2$-$Bi_2O_3$ system" , Mater. Res. Bull., **33**, (1998), 1077-1081.

[16] H.L.TullerIn, H.Tuller, J.Schoonman and I.Riess (Eds.), "Oxygen Ionand Mixed Conductors and their Technological Applications", Kluwer (NATOASI series) ,Dordrecht , **245**, (2000).

[17] John B. Goodenough, J Annu. Rev. Mater. Res. **33,** (2003), 91-128.

[18] W.R. Grove, Phillos.Mag, **41,** (1839), 127-30.

[19] V.V. Kharton, J Mat. Res. Bulletin, **35,** (2000), 515-520.

[20] B.H.C Steele, P.H. Middleton and R.A. Rudkin "Material science aspects of SOFC technology with special reference to anode development", **40-41,** august (1990), 388-393.

[21] A.H. Heuer and L.W. Hobbs, "Advances in Ceramics, Science and Technology of Zirconia", American Ceramic Society, Columbus, **3**, (1981).

[22] M. Mogensen, D. Lybye, N. Bonanos, P.V. Hendriksen and F.W. Poulsen, Solid State Ionics **174,** (2004), 279.

[23] I. Abrahams, Alexandra J. Bush, Simon C.M. Chan and F. Krok, J. Mater. Chem. **11** (2001), 1715-1721.

[24] M.D. Anderson, J.W. Stevenson and S.P. Simner, J. Power Sources, 129, **2**, (2004), 18-22.

[25] Q. Zhu and B. Fan, J. Solid State Ionics, 176, **9-10**, (2005), 889-894.

[26] Naixiong Jiang, Eric D WAchsman, Su-Ho Jung, J. Solid State Ionics, **150,** (2002), 347-353.

[27] Antonino Gulino, Salvatore LA Delfa, and Ignazio Fragala, Chem.Mater, **8, (**1996), 1287-1291.

[28] S. Tekeli, A. Akçimen, O. Gürdal, and M. Gürü, Journal of Achievements in Materials and Manufacturing Engineering, **25,** December (2007).

[29] E.N. Naumovich, J. Solid State Ionics, **93,** (1997), 95-103.

[30] R.N. Vannier, G. Mairesse, F. Abraham, G. Nowogrocki, J. Fouletier and M.Bacmann, J. Solid State Ionics, **78**, (1995), 183-189.

[31] I. Abrahams and F. Krok, J. Mater. Chem., **12,** (2002), 3351-3362.

[32] Bikramjit Basu, Jozef Vleugels, and Omer Van Der Biest, Journal of Alloys and Compounds, **365,** (2004), 266–270.

[33] Bogicevic A. J. Phys Rev.B, **67**, (2003), 24-106.

[34] A.A. Yaremchenko, V.V. Kharton, E.N. Naumovich, A.A. Tonoyan, Materials Research Bulletin, **35** (2000) 515–520.

[35] Midrag Zdujic , Dejan Poleti, Čedomir Jovalekic and Ljiljana Karanovic J. Serb. Chem. Soc., **74,** (12), 1401–1411, (2009) JSCS–3927.

[36] Klaartje De Buysser, Petra Lommens, C. De Meyer, Els Bruneel, Serge Hoste, Isabel Van Driessche Department of Inorganic and Physical Chemistry October , 2004.

[37] E.Pernot, M. Anne, M. Bacmann, P, Strobel, J. Solid State Ionics, **70/71,** (1994), 259-263.

[38] G. C. T. Silva and E. N. S. Muccillo Sixth International Latin-American Conference on Powder Technology, Búzios, Rio de Janeiro, Brazil, **39**, (2004), 1539.

[39] Ying Li, Mingshuai Liu, Jianghong Gong , Yunfa Chen, Zilong Tang, Zhongtai Zhang, Materials Science and Engineering, **103,** (2003), 108.

[40] Yeh-Wu Lao, Shu-Ting Kuo and Wei-Hsing Tuan J Mater Sci: Mater Electron **20, (**2009), 234–241.

[41] Bhadeshia H.K.D.H., "Thermal analyses techniques. Differential thermal analysis", University of Cambridge, Material Science and Metallurgy, July 2010, 170–171.

[42] R. P. W. Scott Physical Chemistry Resources Book V.

[43] E. Barsoukov, J. R. Macdonald (Eds.), Impedance Spectroscopy Theory,Experiment, and Application, 2nd Edition, WILEY, Hoboken, 2005.

[44] J. B. Goodenough, Oxide-ion electrolytes, Annual Review of Materials Research, **33,** (2003) 91–128

[45] Impedance Spectroscopy. R. Macdonald; John Willey (1987).

[46] E.N. Naumovich, J. Solid State Ionics, **93,** (1997), 95-103.

[47] M. Nasraoui, E. Bilal and R. Gibert, Mineral. Mag. **63**, (4), (1999), 567.

[48] M. Zdujic, C. Jovalekic, D. Poleti, L. Karanovic, M. Mitric, " Structural and electrical Properties of the $2Bi_2O_3$. $3ZrO_2$ system," J. Solid State Chemistry, **181,** (2008), 1321-1329.

[49] M.J. Verkerk, A.J.A. Winnubst, A. J. Burggraaf, "Effect of impurities on sintering and Conductivity of yttria-stabilized zirconia," J. Mat. Sci., **17**, (1982), 3113-3122.